Imaging seismic and aseismic plate coupling with interferometric radar (InSAR) in the Hikurangi subduction zone

Louise Maubant[1], William Benjamin Frank[1], Laura Wallace[2], Charles A. Williams[2], and Ian James Hamling[2]

[1]Massachusetts Institute of Technology
[2]GNS Science

July 20, 2023

Abstract

The coupling at the interface between tectonic plates is a key geophysical parameter to capture the frictional locking across plate boundaries, and provides a means to estimate where tectonic strain is accumulating through time. Here, we use both interferometric radar (InSAR) and GNSS data to investigate the plate coupling of the Hikurangi subduction zone beneath the North Island of New Zealand, where multiple slow slip cycles are superimposed on the long-term loading. We estimate the plate coupling across the subduction zone over different observational periods (2, 4, and 10 years) targeting different stages of the slow slip cycles. Our results highlight the importance of the observational period when interpreting coupling maps, notably highlighting the temporal dependence of plate coupling. Through our analysis of multiple geodetic datasets, we demonstrate how InSAR provides powerful constraints on the spatial resolution of plate coupling, even in a region where a dense GNSS network exists.

Imaging seismic and aseismic plate coupling with interferometric radar (InSAR) in the Hikurangi subduction zone

L. Maubant[1], W. B. Frank[1], L.M Wallace[2,3,4],C. Williams[5], Ian Hamling[5]

[1]Department of Earth, Atmospheric and Planetary Sciences, Massachusetts Institute of Technology, Cambridge, MA, USA

[2]University of Texas Institute for Geophysics, Austin Texas

[3]GEOMAR Helmholtz Centre for Ocean Research Kiel, Kiel, Germany

[4]Institute of Geosciences, Christian-Albrechts-Universität zu Kiel, Kiel, Germany

[5]GNS Science, Lower Hutt, New Zealand

Key Points:

- Integration of high-resolution displacement maps from radar imagery captures plate coupling at fine scales
- Estimates of plate coupling depend strongly on the time period over which surface velocities are measured
- Temporal variations in plate coupling highlight when and where slow slip dominates the slip budget

Corresponding author: Louise Maubant, maubantl@mit.edu

Abstract

The coupling at the interface between tectonic plates is a key geophysical parameter to capture the frictional locking across plate boundaries, and provides a means to estimate where tectonic strain is accumulating through time. Here, we use both interferometric radar (InSAR) and GNSS data to investigate the plate coupling of the Hikurangi subduction zone beneath the North Island of New Zealand, where multiple slow slip cycles are superimposed on the long-term loading. We estimate the plate coupling across the subduction zone over different observational periods (2, 4, and 10 years) targeting different stages of the slow slip cycles. Our results highlight the importance of the observational period when interpreting coupling maps, notably highlighting the temporal dependence of plate coupling. Through our analysis of multiple geodetic datasets, we demonstrate how InSAR provides powerful constraints on the spatial resolution of plate coupling, even in a region where a dense GNSS network exists.

Plain Language Summary

Plate coupling as a concept describes to what degree the boundaries between tectonic plates are frictionally locked and building up stress. Such accumulated stress (over many hundreds to thousands of years) will eventually be released in earthquakes, and therefore provides important information about the potential for future earthquakes. Our study uses satellite data to investigate how coupling between the plates along the Hikurangi subduction zone (New Zealand's largest and most dangerous plate boundary fault) changes with time. We analyzed Interferometric Synthetic Aperture Radar (InSAR) and Global Navigation Satellite System (GNSS) data to create maps showing the areas where the plates are stuck together (coupled) and where they move past each other (uncoupled). We show that the locations of plate coupling vary significantly for 2, 4 and 10-year timeframes, highlighting the importance of carefully considering the observation period when interpreting and comparing coupling maps.

1 Introduction

The coupling of tectonic plates describes to what degree the interfaces between them are frictionally locked and building up stress. This tectonic stress will eventually be released episodically once the strength of the fault is surpassed, with the style of slip depending on the fault rheology. Driven by far-field plate motion with a constant velocity V_0, the deformation rate along the plate interface between transient slip events is typically some fraction of the long-term plate motion rate (usually called the slip deficit rate, V). We quantify the degree of plate coupling γ (or the "coupling coefficient") as:

$$\gamma = \frac{V_0 - V}{V_0}. \tag{1}$$

The coupling coefficient varies between 0 and 1, where 1 implies a fully coupled plate interface and 0 suggests continuous motion at the long-term plate rate of one plate relative to the other. By utilizing surface velocity fields estimated from geodetic data, it is possible to recover the distribution of slip deficit rate (or backslip) and interplate coupling across a given fault geometry at depth (Savage, 1983).

The discovery of slow slip more than two decades ago (Dragert et al., 2001) has upended this simple conceptual model of a stationary (e.g., constant slip deficit rate) interseismic phase (e.g., Frank, 2016; Saux et al., 2022; Maubant et al., 2022; Mouchon et al., 2023). Geodetic observations across many tectonic plate boundaries have demonstrated how these transient slip events, which do not radiate seismic waves, can episodically release as much accumulated tectonic stress as major earthquakes (>M7) (e.g., Wallace, 2020; Graham et al., 2016; Maubant et al., 2020). Often (but not always) observed downdip of the seismogenic fault region, past work has highlighted how slow slip can interact with earthquakes by transferring stress onto seismogenically locked portions of the fault (Mazzotti & Adams, 2004; Ito et al., 2013; Kato, 2004; Kaneko et al., 2018).

To assess coupling along subduction zones, surface velocities are typically estimated from campaign or continuous GNSS (Global Navigation Satellite System) surface motion at a given point in space. It follows that the density of the GNSS network then directly informs the potential spatial resolution of the recovered map of plate coupling. Modern SAR (Synthetic Aperture Radar) constellations directly tackle this issue of spatial resolution by measuring ground displacement over hundreds of kilometers with repeat times <24d through Inteferometric Synthetic Aperture Radar (InSAR) analysis. With each pixel of the radar images acting as its own geodetic sensor, this allows for dense spatial coverage of the surface velocity field that complements GNSS (Maubant et al., 2020). The precision of InSAR ground displacement is however much lower than that of GNSS, making it challenging to measure the displacement due to relatively small fault motions, such as a slow slip event.

Thanks to methodological improvements to InSAR processing, we can now constrain small velocities in the InSAR time series with amplitudes of mm/yr (Daout et al., 2019).

Here, we seek to quantify how plate coupling evolves in time and space across the Hikurangi subduction zone beneath New Zealand to capture the interplay between seismic and aseismic regions of frictional locking using both InSAR and GNSS observations. We focus on the Hikurangi margin, which accommodates the oblique subduction of the Pacific plate beneath Australian plate (Nicol et al., 2007), because it hosts multiple regions of slow slip across a range of depths (Wallace & Beavan, 2010; Wallace, 2020; Bartlow et al., 2014) and interact with both local and regional earthquakes (Wallace et al., 2017; Koulali et al., 2017). We consider the deep regions of slow slip to the south west that host major M7 slow slip events lasting 1-2 years, at depths of 25-50 km with a recurrence time of 4-5 years (Figure 1). We also take into account the northern Hikurangi margin's East Coast slow slip events that rupture the shallow, offshore plate interface (Wallace et al., 2016), and are associated with tectonic tremor and increased earthquake activity (Wallace, Beavan, et al., 2012; Delahaye et al., 2009; Todd & Schwartz, 2016). We demonstrate how InSAR can provide high-resolution constraints on the spatial distribution of both aseismic and seismic locking considering different observational time periods during which surface velocities are estimated. With such an approach, we are able to capture the dynamic behavior of a subduction plate interface through time.

2 Geodetic data and analysis

We use the three components of daily positions of 155 continuous GNSS (Global Navigation Satellite System) stations, available between 2006 and 2022 and shown in Figure 1. The data are processed by GeoNet `https://www.geonet.org.nz` with GAMIT software (Herring et al., 2010). To focus on the interseismic geodetic signal, we corrected for co-seismic displacements caused by a March 2021 M7.3 intraslab event located 100 km off the northeast coast in the East Cape area (Figure 1) (Okuwaki et al., 2021). After correction of the co-seismic offset, we observe a post-seismic signal at a few stations that we did not correct (i.e, station WMAT in Figure 1), because the earthquake far from the coast generates a measureable signal at very few stations.

In addition to GNSS data, we use SAR imagery from the Sentinel-1 constellation operated by the European Space Agency. InSAR observations capture surface deformation across large continuous swaths, providing the means to estimate the surface velocity at each of the pixels that make up every radar image; the images analyzed here have a swath width of about 250 km and a length of 400-500 km. Our analysis covers two tracks shown in Figure 1, A081 (ascending, with 183 images) and D175 (descending, with 154 images) that together cover a significant portion of the North Island of New Zealand from October 2014 to January 2022 with repeat times between 6-24 days; we show in Table S1 the number of images and interferograms analyzed in each track.

We use the NSBAS (New Small BAseline Subset) processing chain to process the interferograms that are then unwrapped and inverted to obtain a time series and capture the evolution of surface displacement (Thollard et al., 2021). To ensure robust estimates of the surface displacement time series and minimize potential biases linked to soil moisture and agricultural vegetation, we construct the interferogram network using a combination of short and long-temporal baselines (Mathey et al., 2022; Dodds et al., 2022). To enhance the signal-to-noise ratio, we filter the interferograms using a complex multi-looking with a window size of 64 pixels in range and 16 pixels in azimuth, resulting in a spatial resolution of approximately 160 m $\times$ 240 m. Tropospheric signals are corrected using the ERA-5 reanalysis weather model before unwrapping. Once unwrapped, the interferograms are inverted to obtain the surface displacement time series at each pixel (Doin et al., 2015; López-Quiroz et al., 2009).

3 Estimation of the surface velocity field during over three different time scales

Our objective is to quantify how the plate coupling, inferred from the surface velocity field estimated from the geodetic data, evolves during the interseismic period and superimposed slow slip event cycles. To achieve this, we investigate three different observational time periods (2006-2016, 2018-2022, and 2019.4-2021.3) spanning different portions of the slow slip cycles that occur at the Hikurangi subduction zone. The GNSS dataset covers more than 15 years (2006-2022), while our InSAR dataset covers only the 2014-2022 period. Wallace, Barnes, et al. (2012) utilized campaign GNSS velocities to estimate an average interseismic coupling between 1995-2008. Another study Wallace and Beavan (2010) investigated the coupling between slow slip events for the 2002-2010 period using the horizontal GNSS displacements corrected for observed slow slip. The geodetic data we use here covers a more recent time period with denser spatial coverage that also includes vertical motion, sampling multiple (2-, 4-, and 10-year) time periods to investigate how plate coupling evolves in time.

The continuous GNSS time series from 2006-2022 capture multiple slow slip events at a range of spatiotemporal scales with minimal impact from seasonal environmental signals. Slow slip signals are also evident in our InSAR time series, including events from the Manawatu and Kapiti regions between 2014 and 2015. Because our InSAR time series does not record the beginning of the 2014-2015 deep slow slip event (Wallace, 2020), we are unable to accurately constrain this event with InSAR. We also avoid including the postseismic sequence of the 2016 Kaikōura earthquake and the margin-wide slow slip it triggered (Wallace et al., 2018; Jiang et al., 2018) within the time period of our velocity estimates. We thus use only the InSAR time series between 2018 and 2022 and April 2019 - March 2022. With these data considerations in mind, we estimate the surface velocities from GNSS and InSAR datasets over three different time periods:

- 10-year period between 2006 and 2016 constrained by GNSS displacements,
- 4-year period between 2018 and 2022 constrained by both GNSS and InSAR surface displacements, and
- 2-year period between April 2019 and March 2021 constrained by both GNSS and InSAR surface displacements.

The 2006-2016 period represents the time period before a major neighboring earthquake (the 2016 M7.8 Kaikōura earthquake), 2018-2022 represents the time between deep slow events that recur every four to five years, and April 2019 - March 2022 spans a time period between the major shallow slow events that occur every one to two years.

For each of the above time periods, we estimate a linear velocity V by fitting the following equation with a simple least-squares approach:

$$u(t) = Vt + u_0, \tag{2}$$

where u is the observed displacement, t is time, and u_0 is the static offset of the displacement time series. We estimate the three-component (North, East, and vertical) linear velocity V at each GNSS station. The velocities are projected into an upper plate reference frame using tectonic block Euler poles relative to the ITRF2014 (2014 International Terrestrial Reference Frame) from an elastic block model of the North Island and northern South Island Wallace, Barnes, et al. (2012). Using velocities in a reference frame relative to the upper plate blocks allows us to invert for slip deficit on the plate interface without simultaneously inverting for tectonic rotation of the forearc which is a clear feature of the North Island GNSS velocity field (Wallace et al., 2004).

For each InSAR track, we generate a map of the surface velocity V at each pixel in the satellite's line-of-sight (LOS) (Figure 3). The initial InSAR data is referenced to the ITRF14 reference frame (Stephenson et al., 2022), and we subsequently transform it to the upper plate reference frame used for the GNSS data (as described in the previous paragraph; Figure S2 and S3). To verify that our two datasets are in agreement, we compare the velocity obtained from GNSS data projected into the InSAR LOS direction to the InSAR-derived velocities. The datasets agree well with one another, exhibiting a correlation coefficient of 0.9 (Figure S5).

For the two shorter time periods, we observe higher vertical velocities during the 4-year and 2-year time periods compared to the 10-year period. This difference can be attributed to the larger slip deficit rates between slow slip events during the shorter time periods considered. Comparing the GNSS velocities over the 4-years and 2-year time periods, the only differences we observe are in the region of shallow slow slip events on the East Coast (Figure 2). This region hosts slow slip events that recur every 1-2 years, notably shorter than the 4-year time period. We do not however see a similar difference when comparing the InSAR-derived velocity maps at 2 and 4 years (Figure S6). This is likely because the amplitude of these events in the InSAR are small, InSAR data are more sensitive to the vertical component, and the signal can be hidden in the noise. Because of this observation, the insufficient number of acquisitions during the 2-year observation (maximum 50 dates), and the noise in our time series, we opted to use the 4-year InSAR velocities to constrain both our 2- and 4-years plate coupling models, while still using the 2- and 4-year GNSS velocities for the two respective models (Figure 2).

We estimate the associated error e of our linear velocities for both the GNSS and InSAR datasets as the root-mean-square between the model (Eq. 2) and the time series using the following:

$$e = \sqrt{\frac{\sum_{t=1}^{N}(u(t) - (Vt + u_0))^2}{N}} \tag{3}$$

where N is the number of observation epochs (eq. 2).

4 Geodetic inversion for the plate coupling

To retrieve the distribution of coupling on the Hikurangi subduction interface at depth, we utilize the linear velocities estimated during our three observational time periods to infer the slip rate along the subduction plate interface. We use the velocities estimated at all GNSS stations except those that are influced by volcanic deformation within the Taupo Volcanic Zone of the central North Island, and volcanic-driven deformation at Whakaari/White Island. We now briefly describe our approach to invert for the slip velocity at depth; further details of our inversion are described in the Supplementary Information (Text S3).

We define the model *a priori* (m_0) as a plate interface coupled between 0 and 20 km depth (decreasing with the depth) and uncoupled further below. The poor data resolution near the trench with our terrestrial datasets cannot constrain the coupling near the trench. Consequently the chosen model *a priori* controls the recovered near-trench plate coupling (Figure S11, S12). We do not enforce positivity of the recovered slip velocity: a positive slip rate represents slip deficit (motion in the down-dip direction), while negative slip rates represent forward slip (slip in the updip direction as during a slow slip event). This allows us to obtain a model of the velocity field that accounts for elastic strain accumulation (or release) along the subduction interface for the three observational time periods considered (10, 4, and 2 years).

We invert for the slip rates along a 3D model geometry of the subduction interface (Williams et al., 2013) discretized into a triangle mesh (1746 patches). We use a linear least-squares algorithm with the regularization scheme of Radiguet et al. (2011) to perform the inversion, where two parameters, a damping coefficient (σ_{m0}) and a correlation length (λ), respectively control the stability and spatial smoothness of the recovered solution.

We then introduce a relative weight α to manage the influence of the two geodetic datasets, GNSS and InSAR, where α weights the relative contributions as captured by the covariance matrix of the data (Text S1). To evaluate the impact of each dataset, we separately inverted for the modeled plate coupling using either only GNSS or InSAR displacements (corresponding respectively to α values of 0.001 and 0.999 (Figure S8)). A comparison of the two inverted plate coupling maps shows that the spatial resolving power of InSAR is greater than that of the GNSS data, complementing the higher temporal resolution and lower uncertainties of the GNSS timeseries. We explore different α values to evaluate the best compromise, using a goodness-of-fit χ^2 metric (Figure S10). We choose $\alpha = 0.4$, as it results in the lowest value of the cumulative misfit (sum of χ^2 values for InSAR and GNSS as described in Text S2). After determining the optimal weight, we explore different damping values (σ_{m0}) and correlation length values (λ) to assess the sensitivity of our model to the regularization (see Text S3). With the optimal α value determined, we find the compromise between the misfit of the model (χ^2) and its roughness, which was quantified using the L2 norm for these parameters (Figure S13).

Because the results of our inversion are expressed as slip deficits, we finally divide each patch with the associated value of V_{plate} (2-6 cm/yr; Figure S7) to estimate the coupling coefficient across the subduction zone. Undertaking a least-squares inversion of the surface displacement observations for slip on the plate interface, we obtain estimates of interplate coupling for each of three time periods that we investigate. The predicted surface velocities from the best-fitting slip models compare well with the observed surface velocity fields (Figure S9) for all three time periods.

5 Results and discussion

The recovered plate coupling map for each time period we investigate here are presented in Figure 4. Our 10-year coupling model most representative of the long-term interseismic phase is in good agreement with the model published by Wallace, Barnes, et al. (2012), which used campaign GNSS velocities estimated between 1995 and 2008. We observe low coupling values (γ <0.25) depths >25 km across the margin and an along-strike transition from high coupling coefficients beneath the southern North Island to a largely uncoupled interface beneath the northern and central margin. Such similar long-term coupling over more than two decades (1995-2022) suggests the interseismic phase is relatively stable over long time scales.

The observed surface velocities, which are generally towards the West corresponding to locking at depth, above the deep region of slow slip over the 2006-2016 period are slower relative to the upper plate than the 4- and 2-year velocities estimated at over periods shorter than the regional 4-5 year slow slip recurrence interval. This is not surprising as it is the signature of elastic strain accumulation observed between deep slow slip events in the Kapiti and Manawatu regions (Figure 1). This is captured in our 4- and 2-year coupling models, which aligns closely with past work Wallace and Beavan (2010) that examined coupling between slow slip events during the 2002-2010 period and highlights the stability of the coupling between slow slip events through time. Compared to our 10-year coupling map, this region of coupling extends further downdip (Figure 4), corresponding well with the Kapiti and Manawatu slow slip events that happen at depth (Figure 4). This deep source region of slow slip however appears uncoupled with a null coupling coefficient once we consider our 10-year observational time period, suggesting that all of the accumulated slip deficit is fully relieved by deep slow slip during the 2006-2016 period; this period includes the 2008 Kapiti, the 2010-2011 Manawatu (Wallace & Beavan, 2010), the 2013 Kapiti, and the 2014-2016 Manawatu (Wallace et al., 2014) events.

We observe a difference in coupling within the deep slow slip region of Kapiti and Manawatu between the joint GNSS-InSAR models and those solely constrained by GNSS data at both 4 and 2 years. The joint model reveals a broad coupled region between 30 and 50 km depth, which corresponds to the Manawatu and Kapiti slow slip regions that were constrained previously by estimates of displacements during slow slip (Wallace, 2020) (Figure 4, S11). We note that our plate coupling model based only on GNSS data fails to capture this locked patch with the same level of spatial accuracy. This improved spatial resolution afforded by InSAR is particularly noticeable in areas where the GNSS network is sparse due to the exclusion of stations affected by volcanic signals. Our results thus demonstrate how InSAR can provide high-resolution constraints on plate coupling across a subduction zone, allowing for detailed identification of slow slip source regions (Figure S12). Despite the spatial resolving power of InSAR, the near-trench area of the Hikurangi subduction zone remains poorly resolved (Figure S11, S12). This suggests the importance of offshore geodetic instrumentation in accurately capturing the slip behavior within the tsunamigenic zone near the trench.

We remark that regions of slow slip are typically identified through inversion of static displacements during the slow slip event itself (Frank et al., 2015; Wallace, 2020). The estimation of surface velocities is however a more well constrained problem compare to measuring the displacement between two epochs, allowing us to take full advantage of the InSAR observations. While still possible for the largest slow slip events (Maubant et al., 2020), it would otherwise be challenging to identify where slow slip happens if we solely relied on measuring static displacements with InSAR data. Here we instead identify where slow slip occurs by constraining the slip deficit between slow slip events and comparing this with the longer-term interseismic coupling (Figure 4 and S14); this supposes that the slow slip source region is fully locked in between events. As an example, we map the cumulative slip over one cycle in the deep slow slip region by differencing the predicted slip velocities of our 10-year and 4-year models, shown in Figure 4. We observe that the spatial distribution and maximum slip of about 18 cm corresponds well to past models of slow slip in this region (Williams & Wallace, 2015; Bartlow et al., 2014).

We also observe a difference in coupling over our three observational time periods in the East Coast region of shallow slow slip (Figure 4). During our shortest observational period, we see that the East Coast source region exhibits spatially variable plate coupling, with strong coupling only in the North and the South. Looking at the displacement captured at the coast in Figure 1 (e.g, MAKO), there are multiple slow slip events occurring at <1 yr time scales evident in the GNSS time series. These slow slip events are present within our three observational time periods and thus reduce the recovered coupling in all of our models, explaining this spatially variable coupling within the shallow slow slip source region. At longer time scales (10- and 4-year estimates of plate coupling), this region appears to be fully uncoupled, due to the fact that multiple, shallow east coast SSEs occurred during that period. Unsurprisingly, the East Coast region has a lower coupling (γ <0.30) over 10 years compared to the 2-year and 4-year periods of observation, due to the relatively frequent (every 1-2 years) shallow SSEs.

We observe in Figure 4 an area of negative coupling near the trench in the East Coast region during the 4-year observation period. While the fact that we did not take into account the slow events in the area during this period would explain low or null coupling, it cannot explain negative coupling (more slip than slip deficit during the observational time period). Furthermore, we observe a relatively small coupled patch downdip of this negative coupling that is only present in the 4-year coupling map and not in the 2-year coupling map. We attribute this pair of coupled and uncoupled patches to deformation in the GNSS network due to an earthquake sequence in the neighboring Kermadec subduction zone in March 2021, where we were unable to correct the associated postseismic signal due to the relatively small geodetic signal of the earthquakes far from the geodetic network.

6 Conclusion

We demonstrate here how InSAR data together with GNSS positioning enables us to capture the spatiotemporal evolution of plate coupling in the Hikurangi subduction zone. We show how surface velocities estimated from InSAR time series significantly improves the resolution of slip (deficit) at depth, especially in regions where GNSS coverage is sparse (Figure S8). We highlight that near-trench coupling remains poorly resolved, emphasizing the need for integration of offshore geodetic data (Figure S12). Our plate coupling models estimated over three different time periods (10, 4, and 2 years) are similar to past estimates of coupling constrained solely by GNSS (Wallace & Beavan, 2010; Wallace, Barnes, et al., 2012), but we highlight stark differences with increased spatial resolution of the deep slow slip source region and spatially varying coupling in the East Coast region that depends on the observational time period (Figure S14).

Our results suggest that the interseismic phase is not stationary due to the interplay of multiple slow slip cycles superimposed on the long-term, and likely seismic, coupling (Jolivet & Frank, 2020). This highlights that any estimate of plate coupling, derived from a given time period, is a snapshot of a continuously evolving plate interface (Frank, 2016; Mouchon et al., 2023). We note that the observed agreement between our 10-year model, which most likely represents the long-term interseismic phase, and a previously published interseismic coupling model suggests a relative stability of plate coupling over the past several decades. An advantage of considering several plate coupling models that span different slow slip cycles is that we are able to map out slow slip source regions with robust estimates of surface velocities, rather than noisier measurements of displacement offsets. This allows us to take full advantage of the InSAR dataset and its high spatial resolution, which otherwise lacks the signal-to-noise necessary to estimate the surface displacement offsets during slow slip events. Today, long-term coupling maps ($\geq$20 years) can only be produced using GNSS data. With the increasing duration of current and future SAR constellations, it will be possible to integrate InSAR data into these estimates of long-term coupling to map slip at depth in high resolution. Even with current data limitations, we demonstrate how to resolve in high resolution the interplay of aseismic and seismic regions of coupling across the scale of a subduction zone.

7 Open Research

The GNSS data are in open access on `https://www.geonet.org.nz/data/types/geodetic`. Sentinel-1 data are available online `https://scihub.copernicus.eu`, we provide the results of the coupling maps, and InSAR and GNSS velocities (`https://zenodo.org/record/8124888`).

Acknowledgments

L.M., W.B.F, and L.W. acknowledge support from the National Aeronautics and Space Administration under Grant No. 80NSSC21K0874 issued through the Earth Sciences Division of the Science Mission Directorate. We thank Marie-Pierre Doin for discussions about the processing of the InSAR data.

References

Bartlow, N. M., Wallace, L., Beavan, R. J., Bannister, S., & Segall, P. (2014). Time-dependent modeling of slow slip events and associated seismicity and tremor at the Hikurangi subduction zone, New Zealand. *Journal of Geophysical Research: Solid Earth*, *119*(1), 734–753. doi: 10.1002/2013JB010609

Daout, S., Sudhaus, H., Kausch, T., Steinberg, A., & Dini, B. (2019). Interseismic and Postseismic Shallow Creep of the North Qaidam Thrust Faults Detected with a Multitemporal InSAR Analysis. *Journal of Geophysical Research: Solid Earth*, 1–21. doi: 10.1029/2019JB017692

Delahaye, E., Townend, J., Reyners, M., & Rogers, G. (2009). Microseismicity but no tremor accompanying slow slip in the hikurangi subduction zone, new zealand. *Earth and Planetary Science Letters*, *277*(1-2), 21–28.

Dodds, N., Daout, S., Walker, R., Begenjev, G., Bezmenov, Y., Mirzin, R., & Parsons, B. (2022). Interseismic deformation and strain-partitioning along the main köpetdag fault, turkmenistan, with sentinel-1 insar time-series. *Geophysical Journal International*, *230*(3), 1612–1629.

Doin, M.-P., Lasserre, C., & Grandin, R. (2015). InSAR Processing Sentinel 1 data Case study of subsidence in Mexico city.
doi: 10.5270/Fringe2015.pp116

Dragert, H., Wang, K., & James, T. S. (2001). A silent slip event on the deeper Cascadia subduction interface. *Science*, *292*(5521), 1525–1528. doi: 10.1126/science.1060152

Frank, W. B. (2016). Slow slip hidden in the noise: The intermittence of tectonic release. *Geophysical Research Letters*, *43*(19), 10–125.

Frank, W. B., Radiguet, M., Rousset, B., Shapiro, N. M., Husker, A. L., Kostoglodov, V., ... Campillo, M. (2015). Uncovering the geodetic signature of silent slip through repeating earthquakes. *Geophysical Research Letters*, *42*(8), 2774–2779.

Graham, S., DeMets, C., Cabral-Cano, E., Kostoglodov, V., Rousset, B., Walpersdorf, A., ... Salazar-Tlaczani, L. (2016). Slow Slip History for the MEXICO Subduction Zone: 2005 Through 2011. *Pure and Applied Geophysics*, *173*(10-11), 3445–3465. doi: 10.1007/s00024-015-1211-x

Herring, T., King, R., & McClusky, S. (2010). Introduction to gamit/globk. *Massachusetts Institute of Technology, Cambridge, Massachusetts.*

Ito, Y., Hino, R., Kido, M., Fujimoto, H., Osada, Y., Inazu, D., ... Ashi, J. (2013). Episodic slow slip events in the Japan subduction zone before the 2011 Tohoku-Oki earthquake. *Tectonophysics*, *600*, 14–26. doi: 10.1016/j.tecto.2012.08.022

Jiang, Z., Yuan, L., Huang, D., Zhang, L., Hassan, A., & Yang, Z. (2018). Spatial-temporal evolution of slow slip movements triggered by the 2016 Mw 7.8 Kaikoura earthquake, New Zealand. *Tectonophysics*, *744*(June), 72–81. Retrieved from `https://doi.org/10.1016/j.tecto.2018.06.012` doi: 10.1016/j.tecto.2018.06.012

Jolivet, R., & Frank, W. (2020). The transient and intermittent nature of slow slip. *AGU Advances*, *1*(1), e2019AV000126.

Kaneko, Y., Wallace, L., Hamling, I. J., & Gerstenberger, M. C. (2018). Simple physical model for the probability of a subduction-zone earthquake following slow slip events and earthquakes: Application to the hikurangi megathrust, new zealand. *Geophysical Research Letters*, *45*(9), 3932–3941.

Kato, N. (2004). Interaction of slip on asperities: Numerical simulation of seismic cycles on a two-dimensional planar fault with nonuniform frictional property. *Journal of Geophysical Research: Solid Earth*, *109*(12), 1–17. doi: 10.1029/2004JB003001

Koulali, A., McClusky, S., Wallace, L., Allgeyer, S., Tregoning, P., D'Anastasio, E., & Benavente, R. (2017). Slow slip events and the 2016 Te Araroa Mw7.1 earthquake interaction: Northern Hikurangi subduction, New Zealand. *Geophysical Research Letters*, *44*(16), 8336–8344. doi: 10.1002/2017GL074776

López-Quiroz, P., Doin, M.-p., Tupin, F., Briole, P., & Nicolas, J. M. (2009). Time series analysis of Mexico City subsidence constrained by radar interferometry. *Journal of Applied Geophysics*, *69*(1), 1–15. Retrieved from `http://dx.doi.org/10.1016/j.jappgeo.2009.02.006` doi: 10.1016/j.jappgeo.2009.02.006

Mathey, M., Doin, M.-P., André, P., Walpersdorf, A., Baize, S., & Sue, C. (2022). Spatial heterogeneity of uplift pattern in the western european alps revealed by insar time-series analysis. *Geophysical Research Letters*, *49*(1), e2021GL095744.

Maubant, L., Pathier, E., Daout, S., Radiguet, M., Doin, M.-P., Kazachkina, E., ... Walpersdorf, A. (2020). Independent component analysis and parametric approach for source separation in insar time series at regional scale: Application to the 2017–2018 slow slip event in guerrero (mexico). *Journal of Geophysical Research: Solid Earth*, *125*(3), e2019JB018187.

Maubant, L., Radiguet, M., Pathier, E., Doin, M.-P., Cotte, N., Kazachkina, E., & Kostoglodov, V. (2022). Interseismic coupling along the mexican subduction zone seen by insar and gnss. *Earth and Planetary Science Letters*, *586*, 117534.

Mazzotti, S., & Adams, J. (2004). Variability of near-term probability for the next great earthquake on the cascadia subduction zone. *Bulletin of the Seismological Society of America*, *94*(5), 1954–1959.

Mouchon, C., Frank, W. B., Radiguet, M., Poli, P., & Cotte, N. (2023). Subdaily slow fault slip dynamics captured by low-frequency earthquakes. *AGU Advances*, *4*(4), e2022AV000848.

Nicol, A., Mazengarb, C., Chanier, F., Rait, G., Uruski, C., & Wallace, L. (2007). Tectonic evolution of the active hikurangi subduction margin, new zealand, since the oligocene. *Tectonics*, *26*(4).

Okuwaki, R., Hicks, S. P., Craig, T. J., Fan, W., Goes, S., Wright, T. J., & Yagi, Y. (2021). Illuminating a contorted slab with a complex intraslab rupture evolution during the 2021 mw 7.3 east cape, new zealand earthquake. *Geophysical Research Letters*, *48*(24), e2021GL095117.

Radiguet, M., Cotton, F., Vergnolle, M., Campillo, M., Valette, B., Kostoglodov, V., & Cotte, N. (2011). Spatial and temporal evolution of a long term slow slip event: The 2006 Guerrero Slow Slip Event. *Geophysical Journal International*, *184*(2), 816–828. doi: 10.1111/j.1365-246X.2010.04866.x

Saux, J. P., Molitors Bergman, E. G., Evans, E. L., & Loveless, J. P. (2022). The role of slow slip events in the cascadia subduction zone earthquake cycle. *Journal of Geophysical Research: Solid Earth*, *127*(2), e2021JB022425.

Savage, J. C. (1983). A dislocation model of strain accumulation and release at a subduction zone. *Journal of Geophysical Research*, *88*(B6), 4984–4996. doi: 10.1029/JB088iB06p04984

Stephenson, O. L., Liu, Y.-K., Yunjun, Z., Simons, M., Rosen, P., & Xu, X. (2022). The impact of plate motions on long-wavelength insar-derived velocity fields. *Geophysical*

Research Letters, e2022GL099835.

Thollard, F., Clesse, D., Doin, M.-P., Donadieu, J., Durand, P., Grandin, R., … others (2021). Flatsim: The form@ ter large-scale multi-temporal sentinel-1 interferometry service. *Remote Sensing*, *13*(18), 3734.

Todd, E. K., & Schwartz, S. Y. (2016). Tectonic tremor along the northern hikurangi margin, new zealand, between 2010 and 2015. *Journal of Geophysical Research: Solid Earth*, *121*(12), 8706–8719.

Wallace, L. (2020). Slow slip events in new zealand. *Annual Review of Earth and Planetary Sciences*, *48*, 175–203.

Wallace, L., Barnes, P., Beavan, J., Van Dissen, R., Litchfield, N., Mountjoy, J., … Pondard, N. (2012). The kinematics of a transition from subduction to strike-slip: An example from the central new zealand plate boundary. *Journal of Geophysical Research: Solid Earth*, *117*(B2).

Wallace, L., Bartlow, N., Hamling, I., & Fry, B. (2014). Quake clamps down on slow slip. *Geophysical Research Letters*, *41*(24), 8840–8846.

Wallace, L., & Beavan, J. (2010). Diverse slow slip behavior at the hikurangi subduction margin, new zealand. *Journal of Geophysical Research: Solid Earth*, *115*(B12).

Wallace, L., Beavan, J., Bannister, S., & Williams, C. (2012). Simultaneous long-term and short-term slow slip events at the hikurangi subduction margin, new zealand: Implications for processes that control slow slip event occurrence, duration, and migration. *Journal of Geophysical Research: Solid Earth*, *117*(B11).

Wallace, L., Beavan, J., McCaffrey, R., & Darby, D. (2004). Subduction zone coupling and tectonic block rotations in the north island, new zealand. *Journal of Geophysical Research: Solid Earth*, *109*(B12).

Wallace, L., Hreinsdóttir, S., Ellis, S., Hamling, I., D'Anastasio, E., & Denys, P. (2018). Triggered Slow Slip and Afterslip on the Southern Hikurangi Subduction Zone Following the Kaikōura Earthquake. *Geophysical Research Letters*, *45*(10), 4710–4718. doi: 10.1002/2018GL077385

Wallace, L., Kaneko, Y., Hreinsdóttir, S., Hamling, I., Peng, Z., Bartlow, N., … Fry, B. (2017). Large-scale dynamic triggering of shallow slow slip enhanced by overlying sedimentary wedge. *Nature Geoscience*, *10*(10), 765–770.

Wallace, L., Webb, S. C., Ito, Y., Mochizuki, K., Hino, R., Henrys, S., … Sheehan, A. F. (2016). Slow slip near the trench at the hikurangi subduction zone, new zealand.

Science, *352*(6286), 701–704.

Williams, C. A., Eberhart-Phillips, D., Bannister, S., Barker, D. H., Henrys, S., Reyners, M., & Sutherland, R. (2013). Revised interface geometry for the hikurangi subduction zone, new zealand. *Seismological Research Letters*, *84*(6), 1066–1073.

Williams, C. A., & Wallace, L. M. (2015). Effects of material property variations on slip estimates for subduction interface slow-slip events. *Geophysical Research Letters*, *42*(4), 1113–1121.

Figure 1: Tectonic setting of the Hikurangi subduction zone. The blue and red contours are 100mm contour slip intervals of slow slip events for 2002-2014 period (Wallace, 2020). The blue contours represent deep (25-40 km) and long-term (1-2 years) slow slip events that occurred in the Kapiti and Manawatu regions, while the red contours represent shallow (<15 km) and short-term (a few to several weeks) slow slip events that occurred offshore the East Coast. Black lines: crustal faults, Red dots: continuous GNSS stations (GeoNet network). Dashed dark black lines indicate the depths to the Hikurangi subduction interface in kilometers below sea level (Williams et al., 2013). The black boxes represent the footprint of the two tracks used in this study (Asc081 and Desc175). Beach balls is the moment tensor of the East Cape (Mw 7.3, 03/04/21). Below: Several GNSS time series from our study region (KAPT, TAKP, CKID, MAKO, and WMAT). The east displacement on TAKP and KAPT exhibits long-term transient events, including slow slip and afterslip following the Kaikōura earthquake in the Kapiti region. The east displacement on WMAT, MAKO, and CKID illustrates the interplay of multiple slow slip cycles. The red lines denote the Kaikōura (2016/11/14) and Kermadec (2021/03/04) earthquakes.

Figure 2: GNSS velocities over different time periods. a) Velocities between 2006 and 2016 (10 years). b) Velocities between 2018 and 2022 (between), corresponding to the period between deep a slow slip events. c) Velocities between April 2019 and March 2021, corresponding to the period between major slow slip events. The color scale indicates the magnitude of the velocities in millimeters per year for the vertical component. d) Difference between the 10-year (a) and 2-year (b) velocities.

Figure 3: Surface velocities over 2018-2022 between deep slow slip events. Top: a) and b) InSAR velocity maps for the respsective ascending and descending tracks. The red dots on the ascending map represent the GNSS locations of TAKP and LEYL stations, which are shown below. Bottom: c) and d) East displacement time series respsectively at TAKP and LEYL. The dashed red lines in c and d represent the estimated velocities over 2018-2022 (TAKP) and over the period April 2019 - March 2021 (LEYL). e) and f) Comparison of the A081 track displacements (blue dots) and the GNSS projected into Line-Of-Sight (LOS) (black dots). g) and h) Comparison of the D175 track displacements (blue dots) and the GNSS projected into LOS (black dots). The blue lines in these four panels represent a smoothing of the InSAR displacements over three epochs.

Figure 4: Plate coupling maps of the Hikurangi subduction zone for the three analyzed time periods. a) Coupling between deep slow slip events estimated over 4 years using InSAR and GNSS. b) Coupling between major deep and shallow slow slip events estimated over 2 years using InSAR and GNSS. c) Coupling representative of the interseismic period over 10 years using only GNSS data. The blue lines are the slip contour of the SSEs between 2002 and 2014, black lines are the footprint of the two InSAR tracks. d) Profiles of the coupling coefficient as a function of depth along the AA' and BB' profiles shown in c. The orange, blue and red lines are respectively the coupling over the 10-, 4-, 2-year periods. Red squares are the slow slip events regions e) Difference in coupling over 4 years between the InSAR-only and the GNSS-only models. f) Difference of slip deficit over 4 years, corresponding to one deep slow slip cycle, using the velocities predicted by our 10- and 4-year models. Unresolved patches are transparent using the resolution matrix of the 10-yr model.

Figure 1.

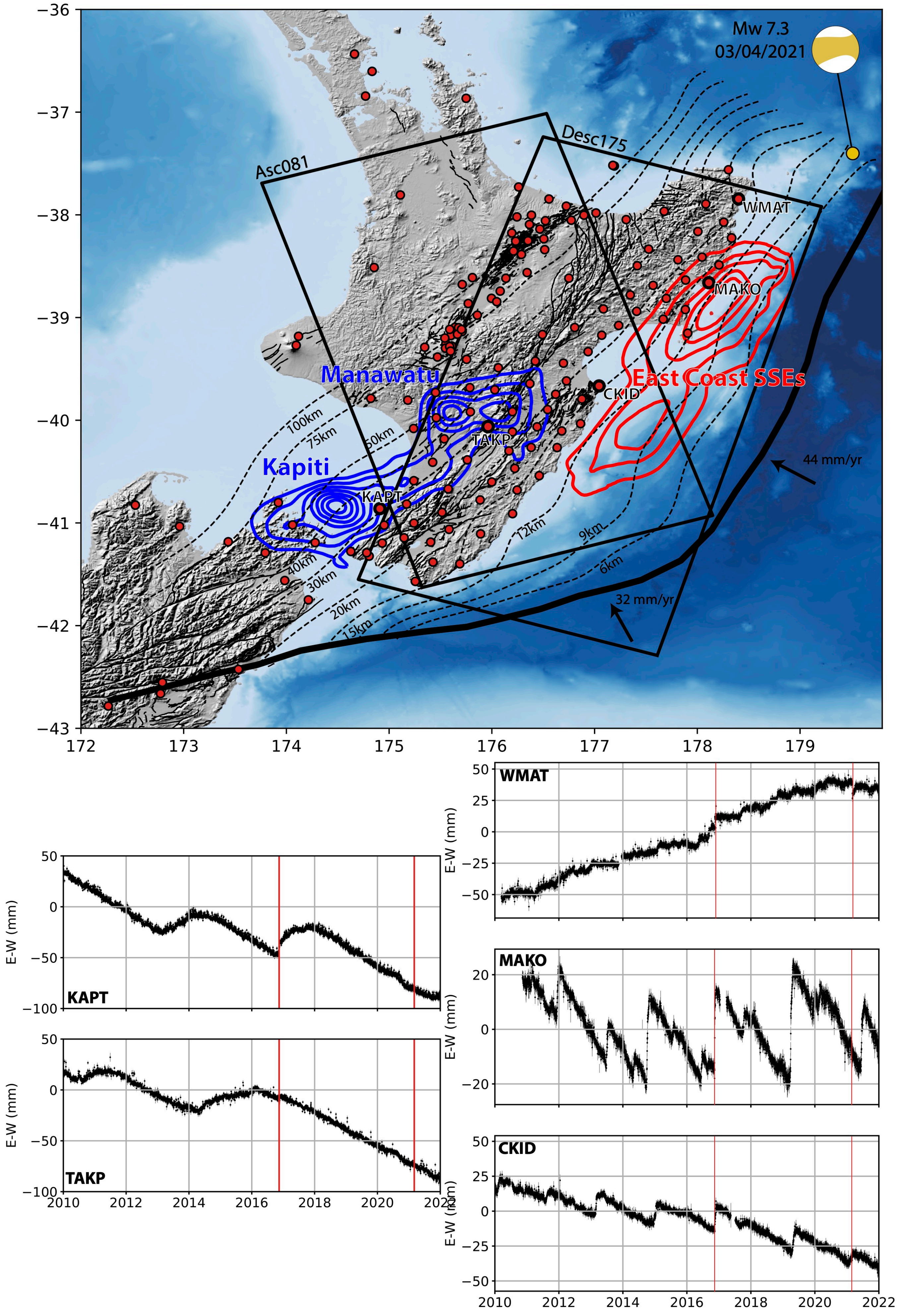

Mw 7.3
03/04/2021
Asc081
Desc175
WMAT
MAKO
CKID
TAKP
KAPT
Manawatu
Kapiti
East Coast SSEs
44 mm/yr
32 mm/yr
100km
75km
50km
40km
30km
20km
15km
12km
9km
6km
WMAT
MAKO
CKID
KAPT
TAKP
E-W (mm)

Figure 2.

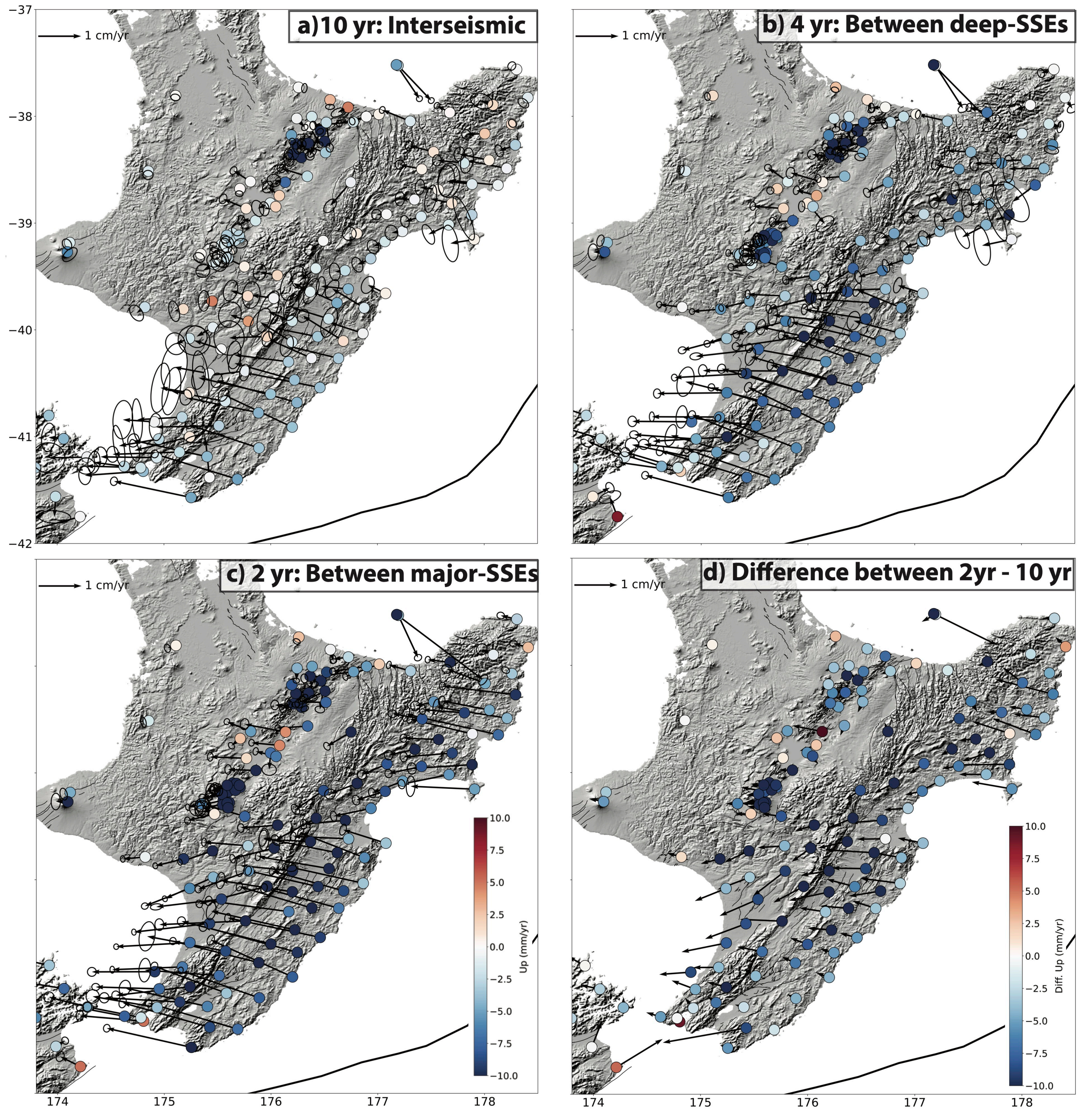

a)10 yr: Interseismic
b) 4 yr: Between deep-SSEs
c) 2 yr: Between major-SSEs
d) Difference between 2yr - 10 yr
1 cm/yr
Up (mm/yr)
Diff. Up (mm/yr)
−37
−38
−39
−40
−41
−42
174
175
176
177
178
10.0
7.5
5.0
2.5
0.0
−2.5
−5.0
−7.5
−10.0

Figure 3.

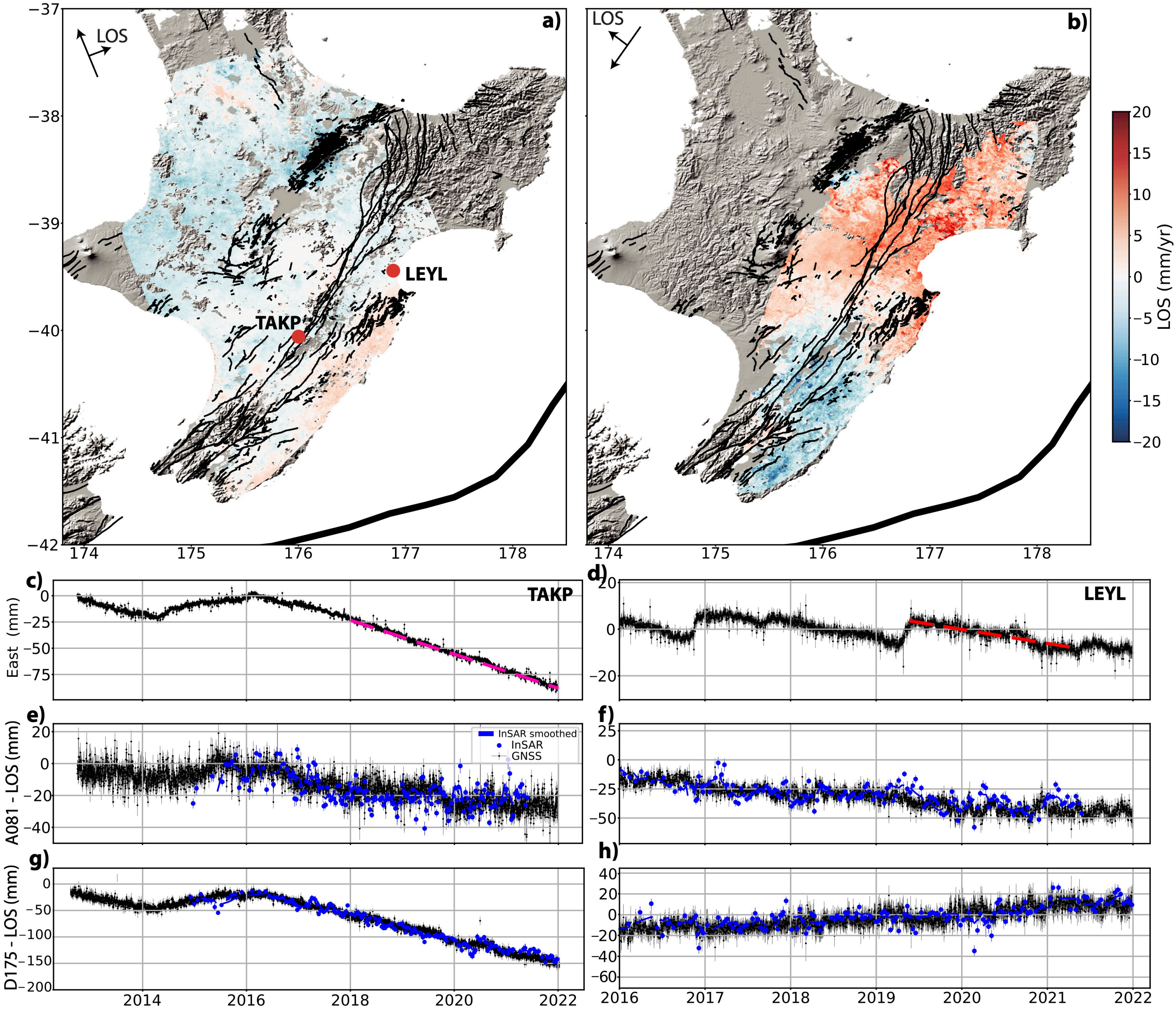

a)
b)
LOS
TAKP
LEYL
LOS (mm/yr)
c)
d)
e)
f)
g)
h)
East (mm)
A081 - LOS (mm)
D175 - LOS (mm)
InSAR smoothed
InSAR
GNSS

Figure 4.

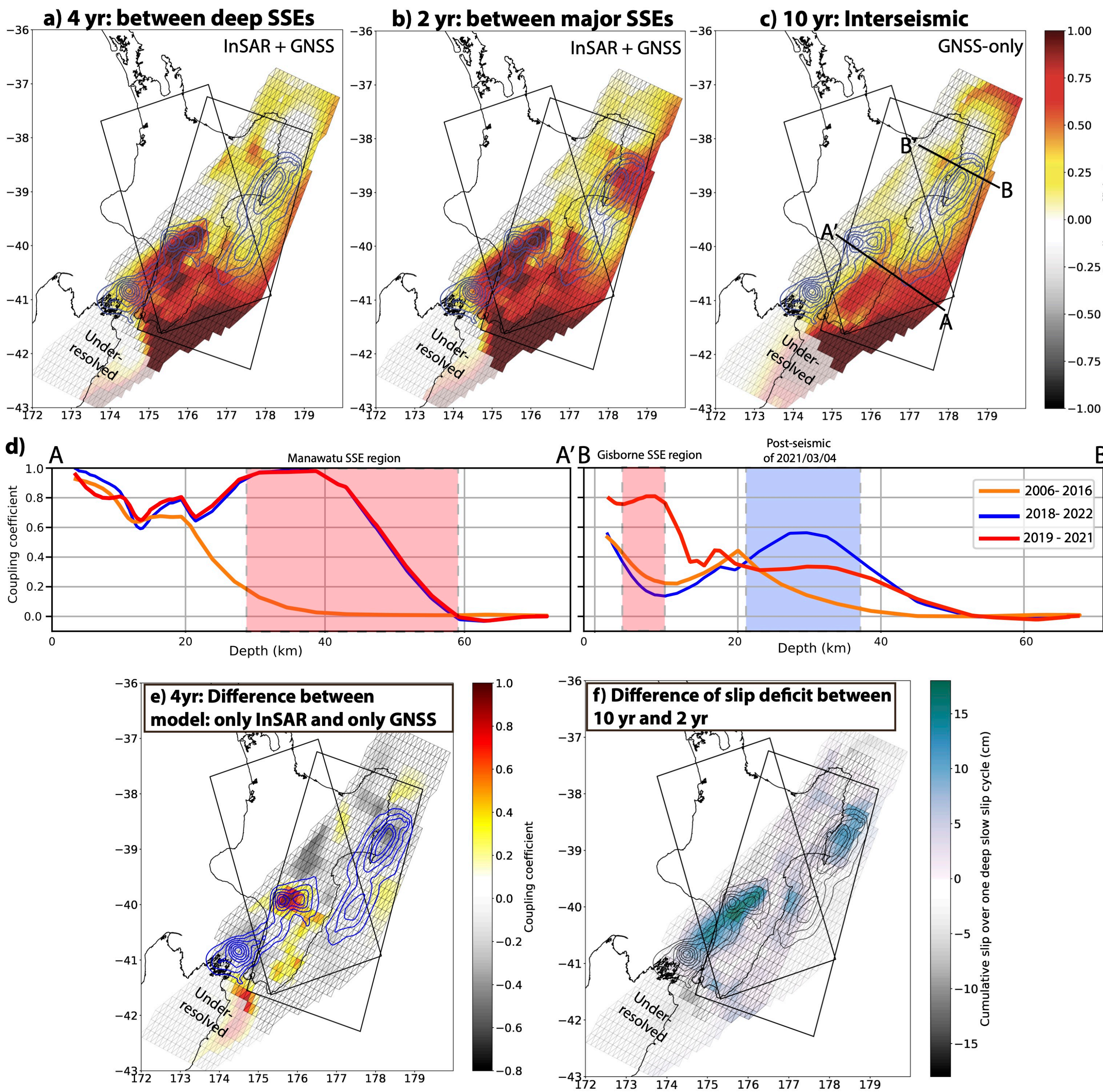

a) 4 yr: between deep SSEs
InSAR + GNSS
b) 2 yr: between major SSEs
InSAR + GNSS
c) 10 yr: Interseismic
GNSS-only
Under-resolved
Coupling coefficient
d)
A
A′
Manawatu SSE region
B
B′
Gisborne SSE region
Post-seismic of 2021/03/04
2006- 2016
2018- 2022
2019 - 2021
Coupling coefficient
Depth (km)
e) 4yr: Difference between model: only InSAR and only GNSS
f) Difference of slip deficit between 10 yr and 2 yr
Cumulative slip over one deep slow slip cycle (cm)

Supporting Information for "Imaging seismic and aseismic plate coupling with interferometric radar (InSAR) in the Hikurangi subduction zone"

L. Maubant[1], W. B. Frank[1], L.M Wallace[2,3,4],C. Williams[5], Ian Hamling[5]

[1]Department of Earth, Atmospheric and Planetary Sciences, Massachusetts Institute of Technology, Cambridge, MA, USA

[2]University of Texas Institute for Geophysics, Austin Texas

[3]GEOMAR Helmholtz Centre for Ocean Research Kiel, Kiel, Germany

[4]Institute of Geosciences, Christian-Albrechts-Universität zu Kiel, Kiel, Germany

[5]GNS Science, Lower Hutt, New Zealand

Contents of this file

1. Text S1 to S3
2. Figures S1 to S14
3. Tables S1

Text S1. Definition of the dataset weighting coefficient

The relative weight between the two datasets is introduced by a weighting factor of the data covariance matrix, C_d:

$$C_d = \begin{bmatrix} \alpha^2 C_{dInSAR} & 0 \\ 0 & (1-\alpha)^2 C_{dGNSS} \end{bmatrix} \tag{1}$$

where C_{dGNSS} is the covariance of the GNSS data, C_{dInSAR} is the covariance of the InSAR data and α is the weighting coefficient. If $\alpha = 0$ the weight of the InSAR data is null, if α=1 the weight of the GNSS data is null.

Text S2. Choice of weighting coefficient

We evaluate a range of values of α, the weighting coefficient between the GNSS and InSAR datasets, between 0.2 and 0.9. We observe that the goodness-of-fit χ^2 value of each dataset is less than 0.4 and does not change significantly with α. This suggests that this range of α values is a reasonable, with both datasets fitting well the predictions. Models with different weights within this broad range are all quite similar to one another. However, if the weight exceeds α=0.6, we are not able to resolve the plate coupling in the North of the subduction, because we do not have InSAR data in this region. We chose a value of 0.4 because it is a reasonable balance between the two datasets and produces a model with a low χ^2 value.

Text S3. Inversion method

We used a static inversion method to estimate the slip deficit rates on the subduction interface based on the observed displacement rates on the surface (Savage, 1983). The map of predicted velocities on the plate interface recovered using this inversion represents the estimated slip deficit rate. To obtain the coupling coefficient we need to divide each patch result by the loading velocity:

$$\gamma = \frac{V_{backslip}}{V_0}. \tag{2}$$

We use the model of Wallace and Beavan (2010) to estimate V_0 (Figure S6). Plate coupling (γ), where the subducting plate is assumed to be frictionally locked to the upper plate, is typically <1, with 1 designating a fully locked interface. A negative or null value of coupling corresponds to slip on the interface during the observational period; values of slip are typically higher than V_0, producing coupling values < -1.

In our forward model, the Green's functions are computed for a homogeneous elastic half-space using the analytical formulation of Okada (1992). To alleviate the inversion's computational cost, we reduce the number of InSAR velocity measurements in each track by performing a uniform downsampling pixel values with a 10×10 km^2 window. The associated InSAR uncertainties are computed from the errors associated with each pixel (Figure S5) using the same downsampling method. We neglect the covariance between pixels, and covariance terms between our GNSS and InSAR datasets in this inversion to reduce the computational cost. We note that considering the covariance between pixels and the covariance terms between our GNSS and InSAR datasets in the inversion would lead to excessive downweighting of the InSAR data, likely undervaluing InSAR's contribution to the overall analysis (Bekaert et al., 2016). The slip direction is fixed in the inversion using the rake of the block model that defines our upper plate reference frame (Wallace & Beavan, 2010), where the rake of each fault patch is the projection of the plate velocity vectors from the block model (Figure S6). Finally to calculate our model m, we perform a linear inversion:

$$m^* = m_0 + C_m G^t (G C_m G^t + C_d)^{-1} (d - G m_0) \tag{3}$$

where m_0 is the model *a priori* (Tarantola, 2005), and C_d and C_m are respectively the covariance matrices of the data and the model.

The purpose of utilizing the model covariance matrix C_m is to incorporate correlation between adjacent parameters, which is known as spatial smoothing. The value at position (i, j) in C_m is determined by the following equation:

$$C_m(i,j) = (\sigma_{m0}\frac{\lambda_0}{\lambda})^2 exp(-\frac{d(i,j)}{\lambda}) \tag{4}$$

We explore the optimal values of σ_{m0} and λ for each time periods. For the 2- and 4-years, we first explore the optimal value of $\log_{10}(\sigma_{m0}) = -2.6$ for a fixed λ=50 km. Once the optimal value is found (Figure S13) we then search for the optimal λ value which we fix to λ=30 km. The optimal model has a $\chi^2 = 0.21$ (2-year) and $\chi^2 = 0.25$ (4-year). For the 10-year observational period where we only use GNSS data, we search for different optimal values (Figure S11, $\log_{10}(\sigma_{m0}) = -1$ and $\lambda = 30$km).

References

Bekaert, D. P., Segall, P., Wright, T. J., & Hooper, A. J. (2016). A Network Inversion Filter combining GNSS and InSAR for tectonic slip modeling. *Journal of Geophysical Research: Solid Earth*, *121*(3), 2069–2086. doi: 10.1002/2015JB012638

Okada. (1992). Internal deformation due to shear and tensile faults in a half space. *Bulletin of the Seismological Society of America*, *82*(2), 1018–1040. Retrieved from `http://bssa.geoscienceworld.org/content/82/2/1018.short`

Savage, J. C. (1983). A dislocation model of strain accumulation and release at a subduction zone. *Journal of Geophysical Research*, *88*(B6), 4984–4996. doi: 10.1029/JB088iB06p04984

Tarantola, A. (2005). *Inverse problem theory and methods for model parameter estimation*. Society for Industrial and Applied Mathematics.

Wallace, L., & Beavan, J. (2010). Diverse slow slip behavior at the hikurangi subduction margin, new zealand. *Journal of Geophysical Research: Solid Earth*, *115*(B12).

Table S1. Table of the number of images and interferograms for two Sentinel-1 tracks used in this study.

Track Name	Number of Images	Number of Interferograms
A081	183	1376
D175	154	1281

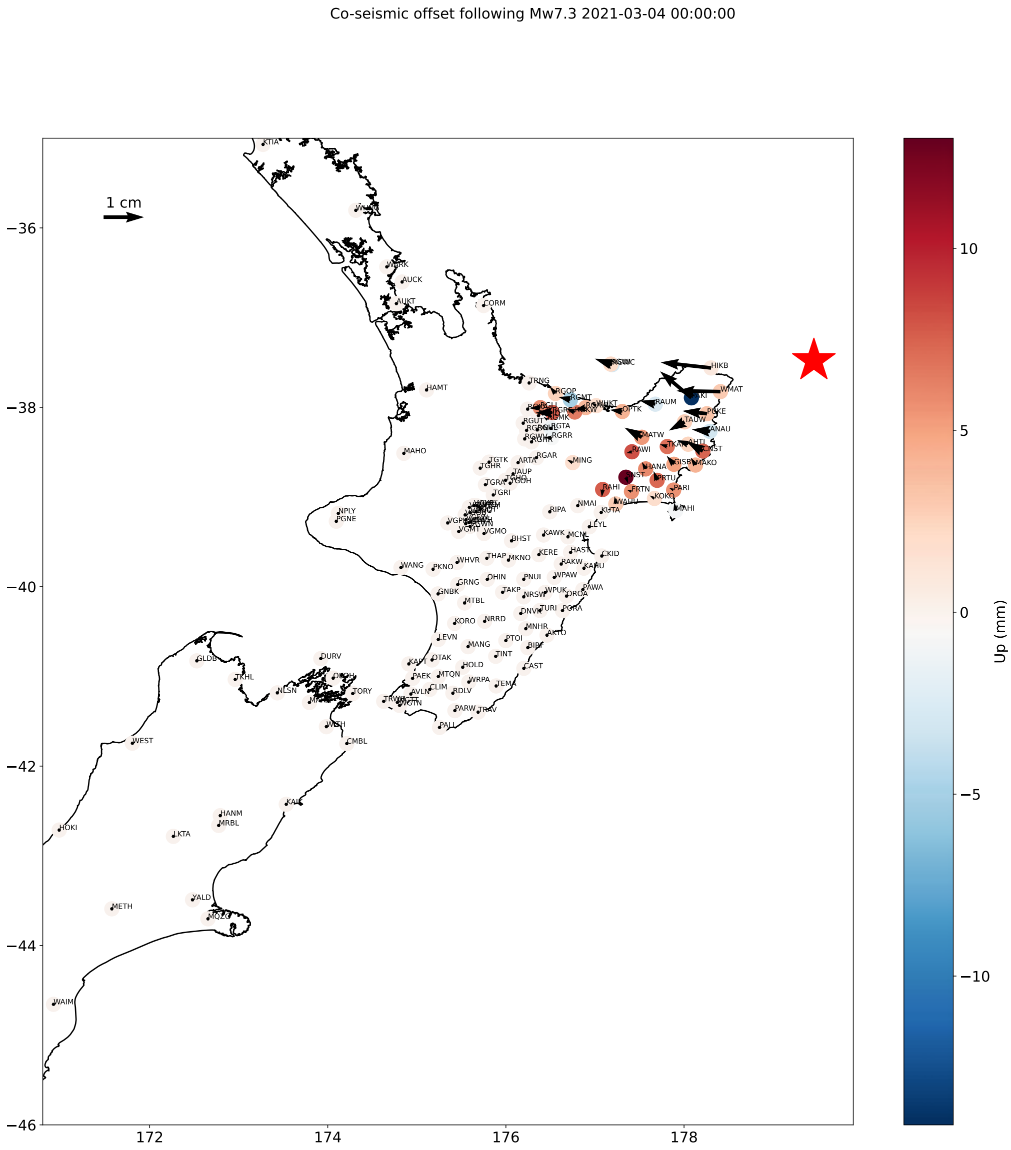

Figure S1. Coseismic offset corrected from GNSS stations for the seismic sequence of March, 4th, 2021.

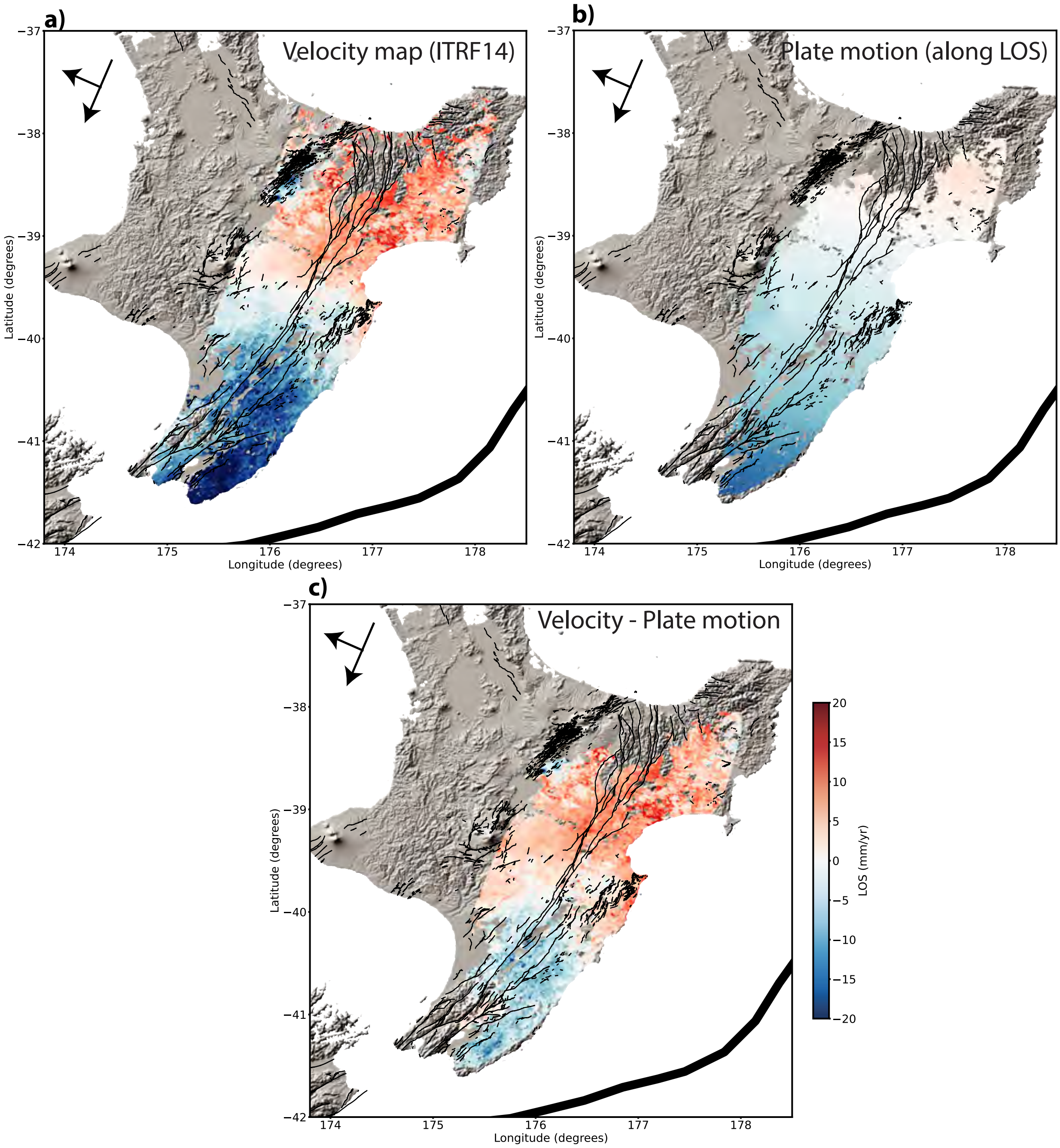

Figure S2. D175 velocity maps. a) Velocity map in ITRF14 reference frame, b) Plate motion in Line-Of-Sight of the satellite. c) Velocity map corrected from the plate motion

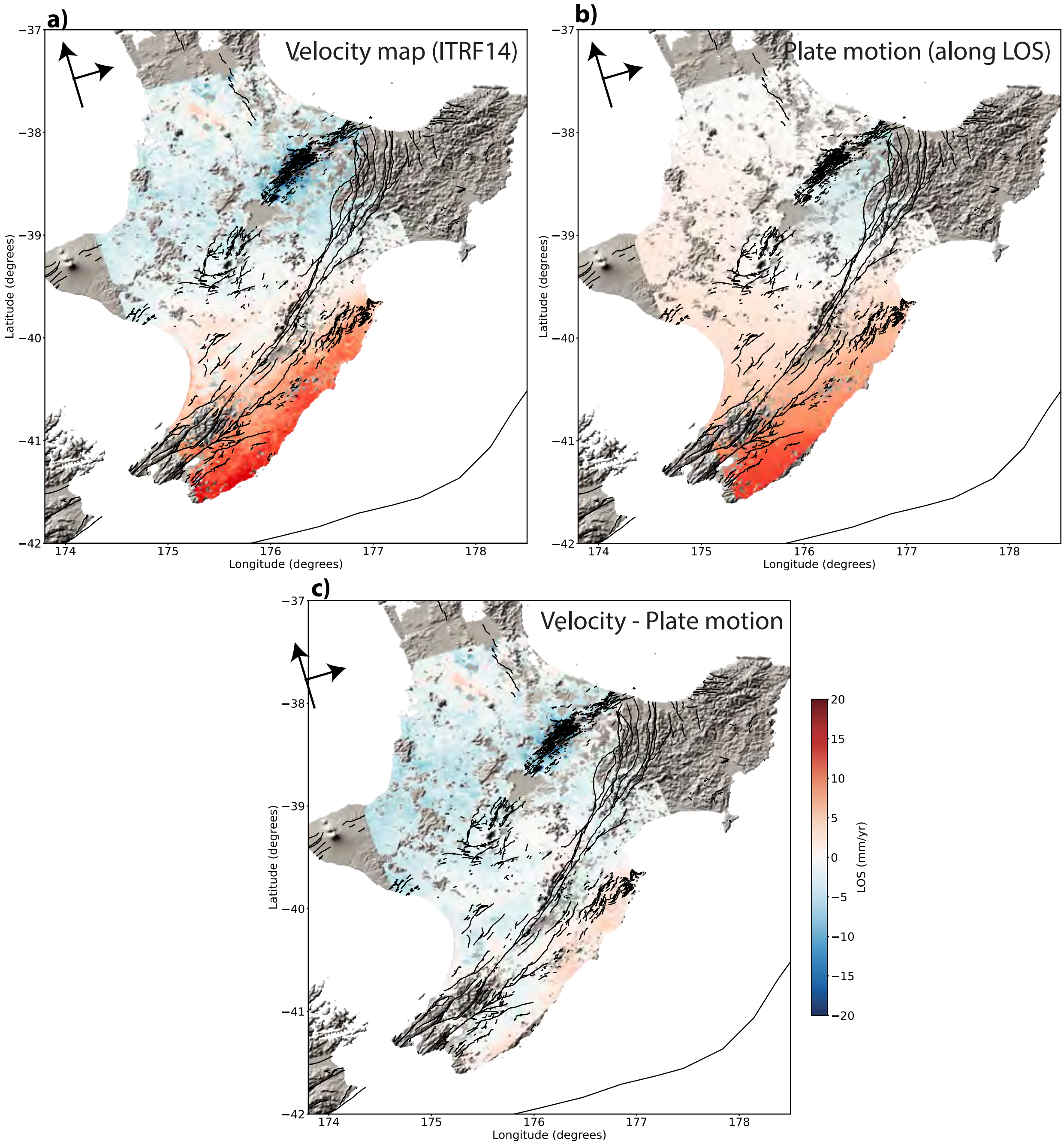

Figure S3. A081 velocity maps. a) Velocity map in ITRF14 reference frame, b) Plate motion in Line-Of-Sight of the satellite. c) Velocity map corrected from the plate motion

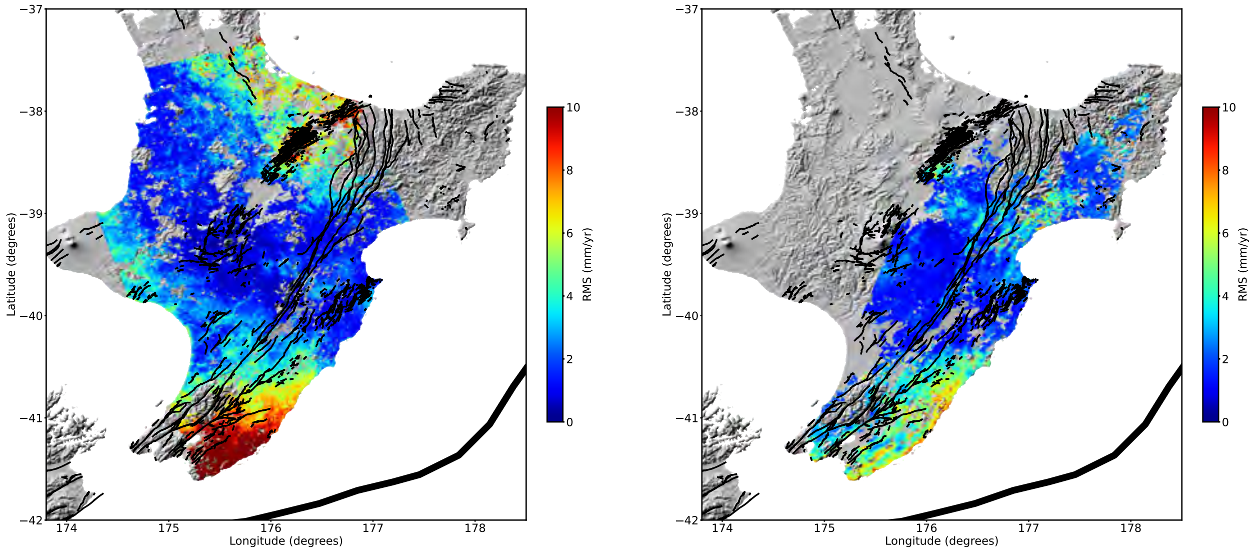

Figure S4. Errors associated to each pixel for InSAR velocity maps. Left: RMSE of A081 track. Right: RMSE of D175 track.

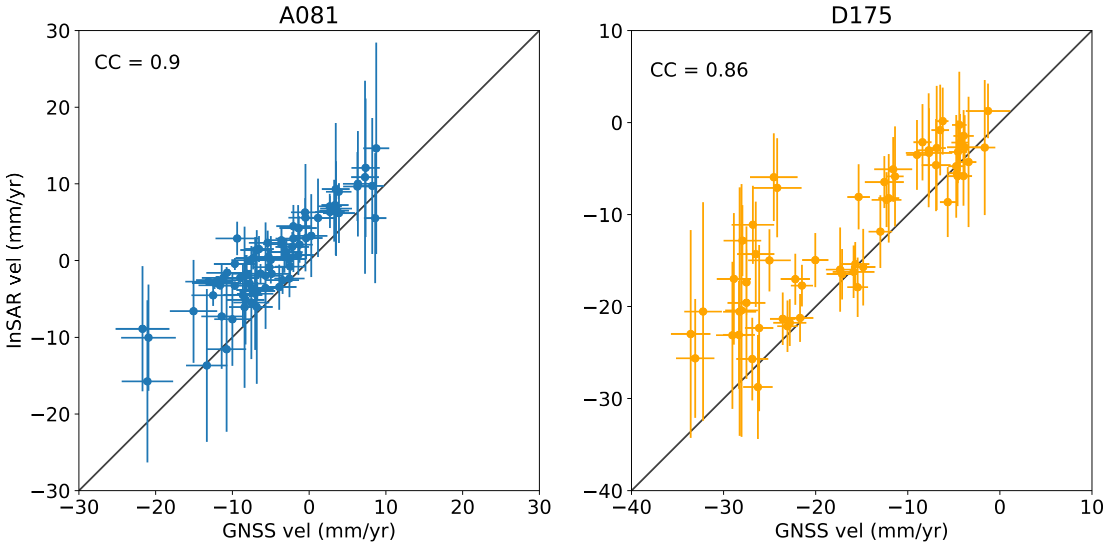

Figure S5. Comparison between InSAR and GNSS velocities (converted in LOS). Left: comparison for the ascending track. Right: comparison for the D175 track.

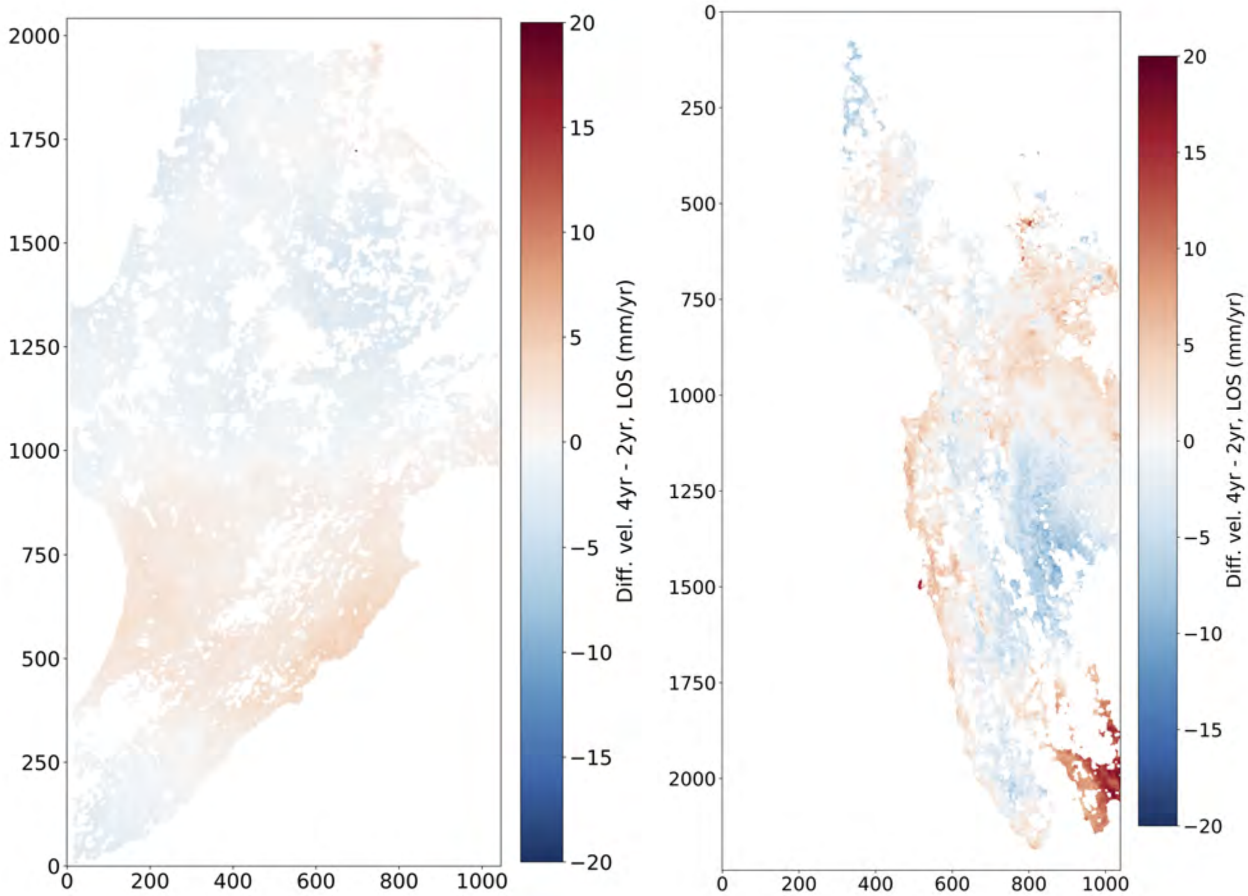

Figure S6. Difference between InSAR velocities maps calculated on a period of 4 years and a period of 2 years. Left: ascending track, right: descending track.

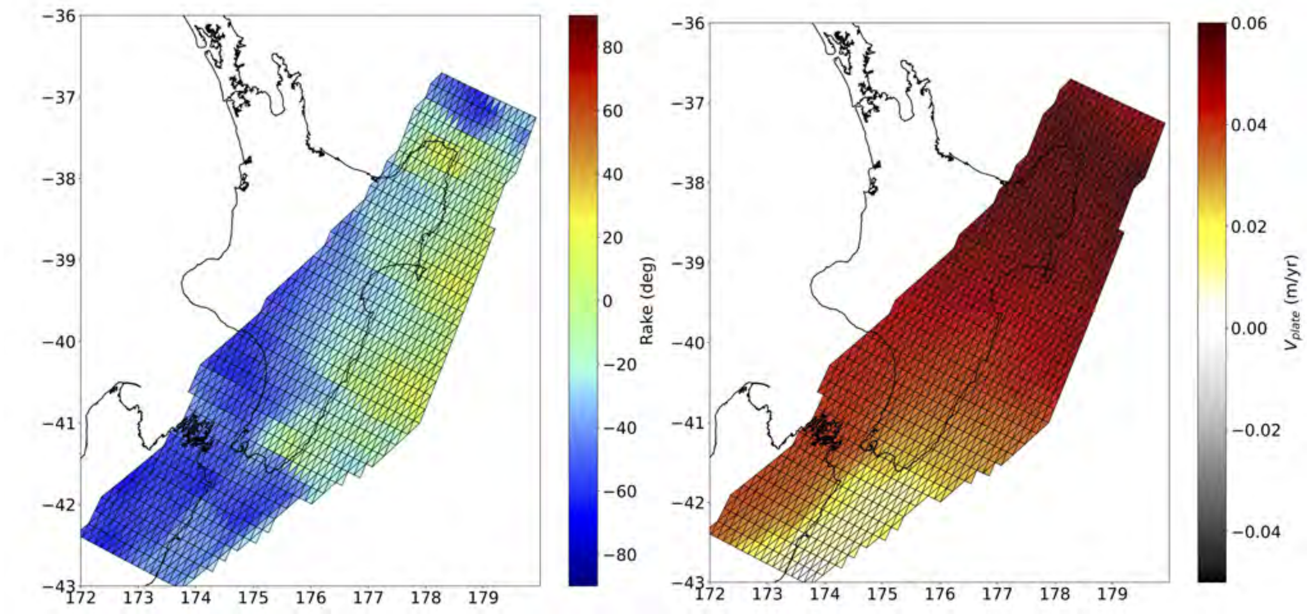

Figure S7. Rake (left) and velocity plate (right) model of the Hikurangi subduction zone from (Wallace & Beavan, 2010).

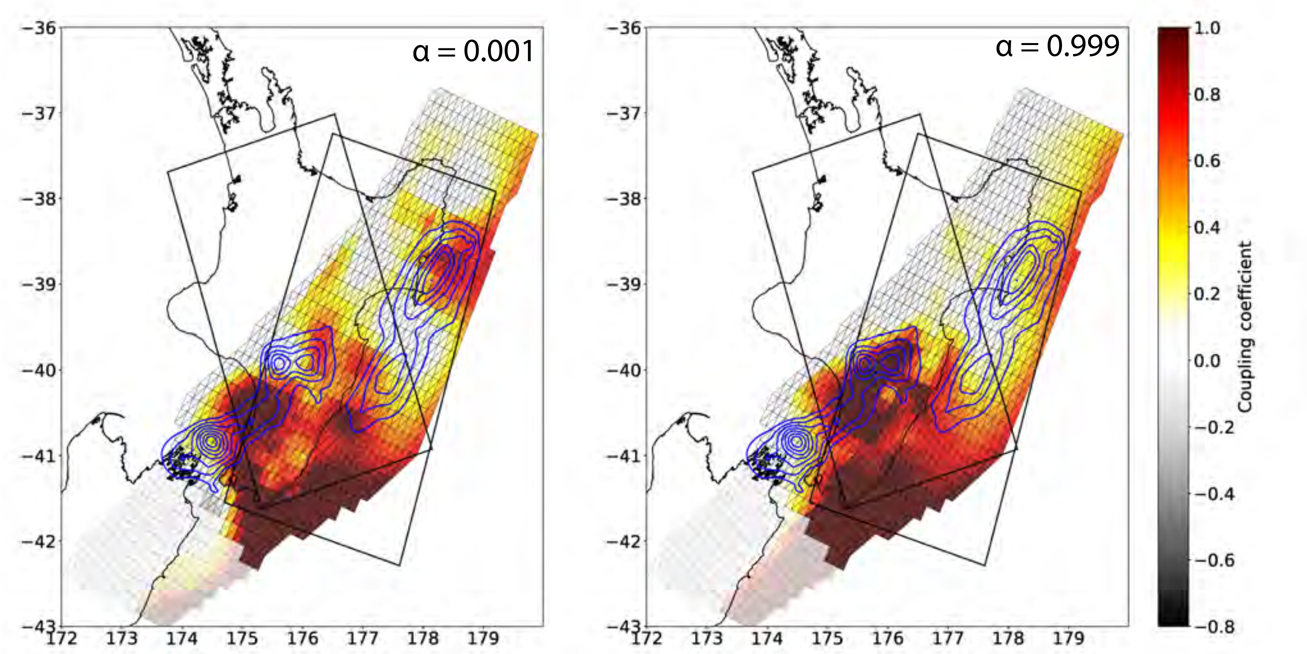

Figure S8. Model of coupling between deep slow slip events (2-years) using only GNSS data on the left ($\alpha = 0.001$) or only InSAR data on the right ($\alpha = 0.999$). The blue lines represent the slow slip events. The black rectangles are the footprint of the InSAR tracks.

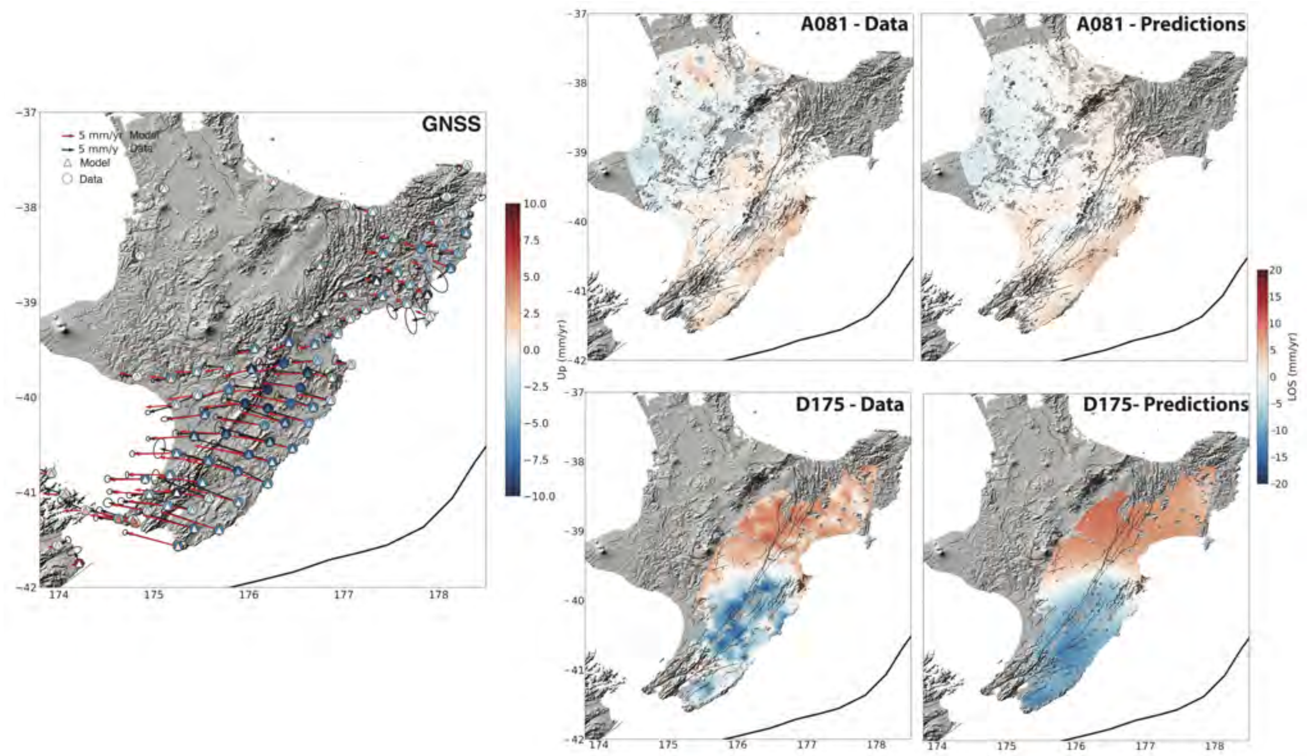

Figure S9. Comparison between data and predictions of the model for the inversions of 2-years of observational period. The Left panel is the GNSS data (black arrows and circles) and prediction (red arrows and triangles). The right panels are data and predictions for InSAR data (A081 on up line, D175 on bottom line).

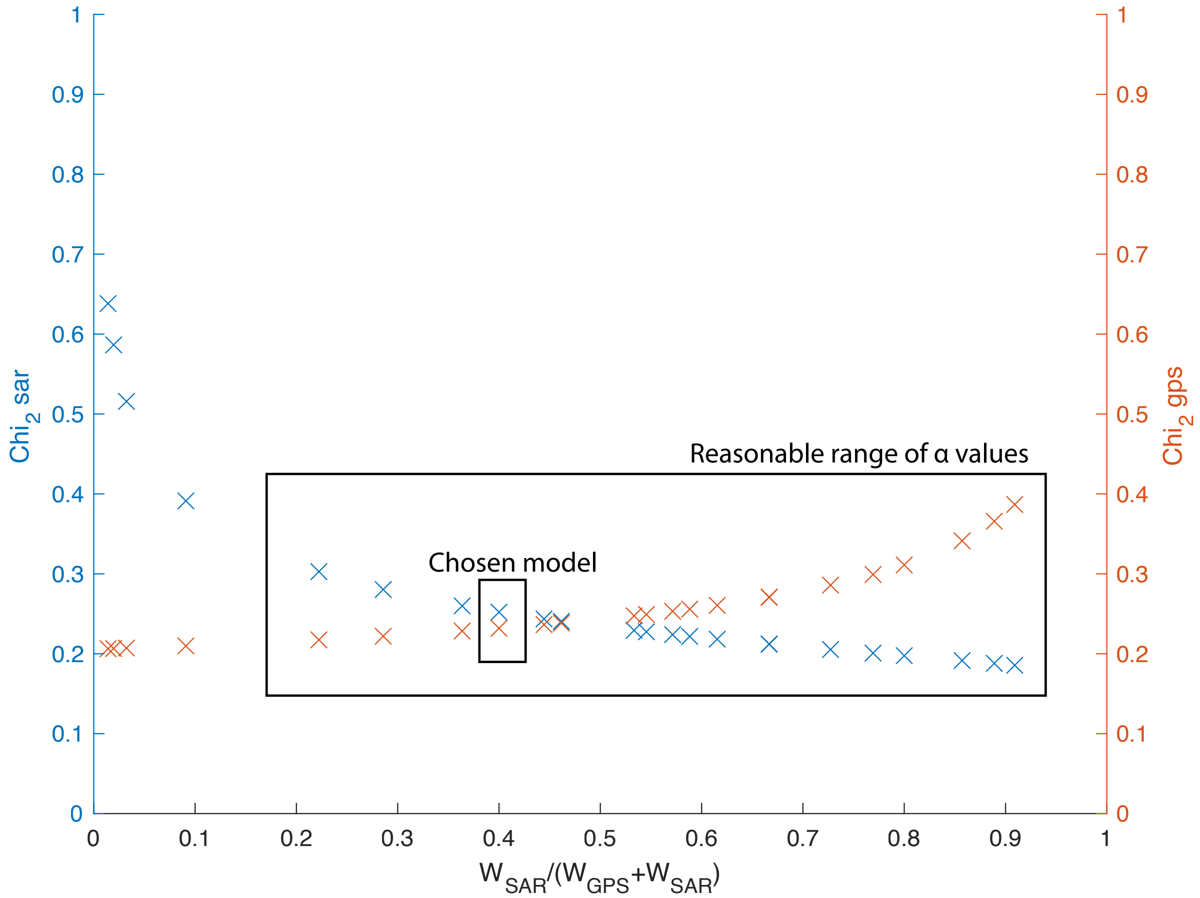

Figure S10. χ^2 values for InSAR (in blue) and GNSS (in orange) as function of the weight (α). The chosen model is framed in black (small rectangle).

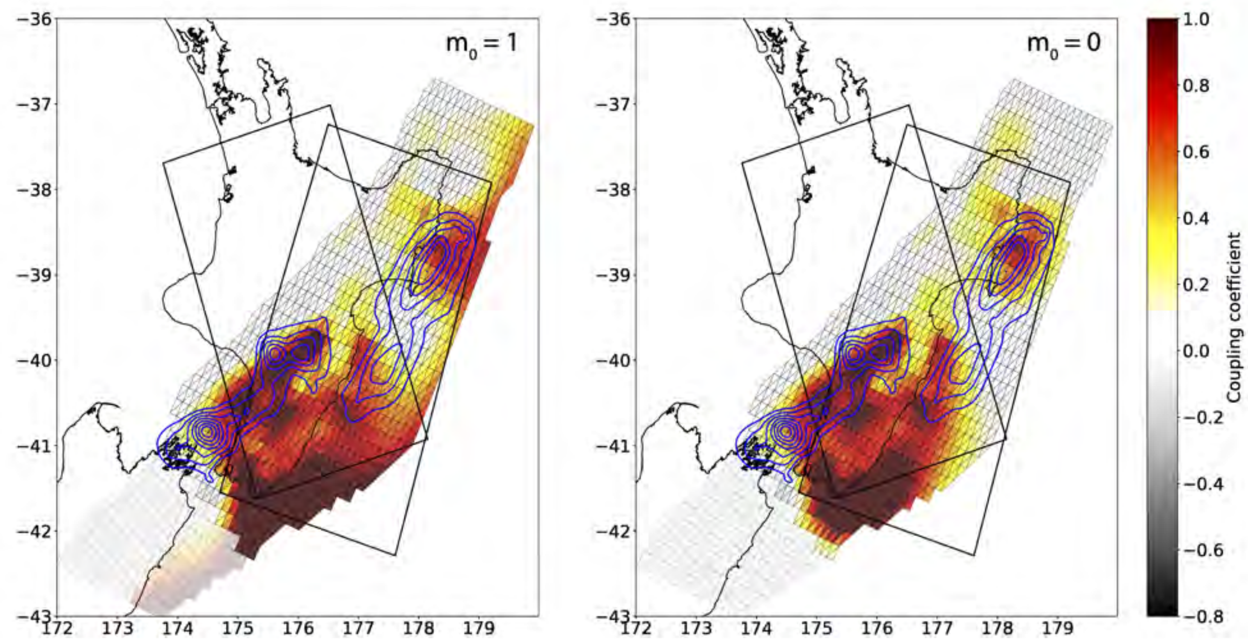

Figure S11. Model of coupling between deep slow slip events (2-years) using a model a priori coupled (left) or uncoupled (right). The blue lines represent the slow slip events. The black rectangles are the footprint of the InSAR tracks.

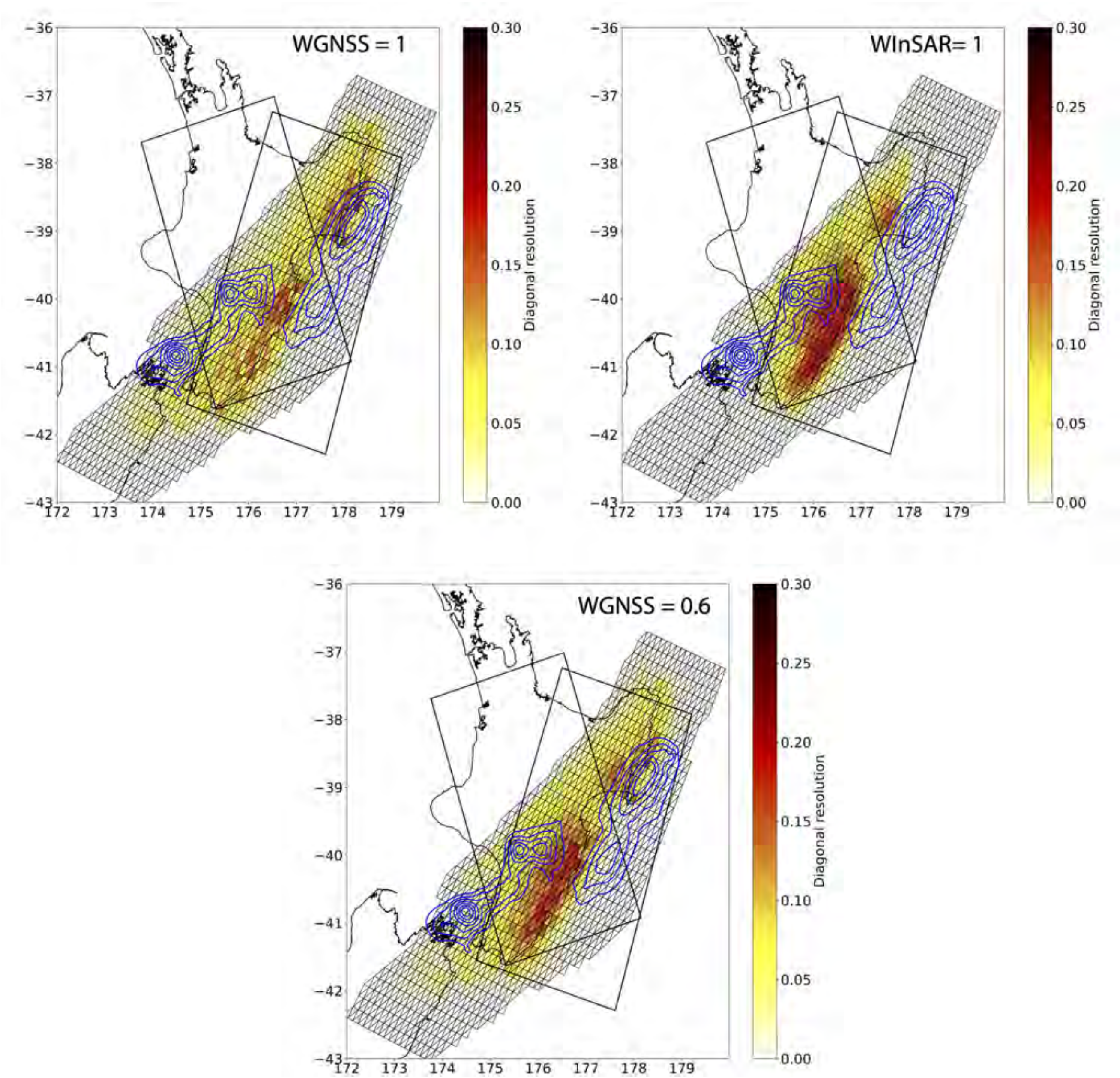

Figure S12. Diagonal of the matrix of resolution for: (right) a model with an α 0.001 (GNSS only); (left) a model with an α 0.999 (InSAR only) and (bottom) our chosen model (α=0.4). The model a priori m_0 is coupled.

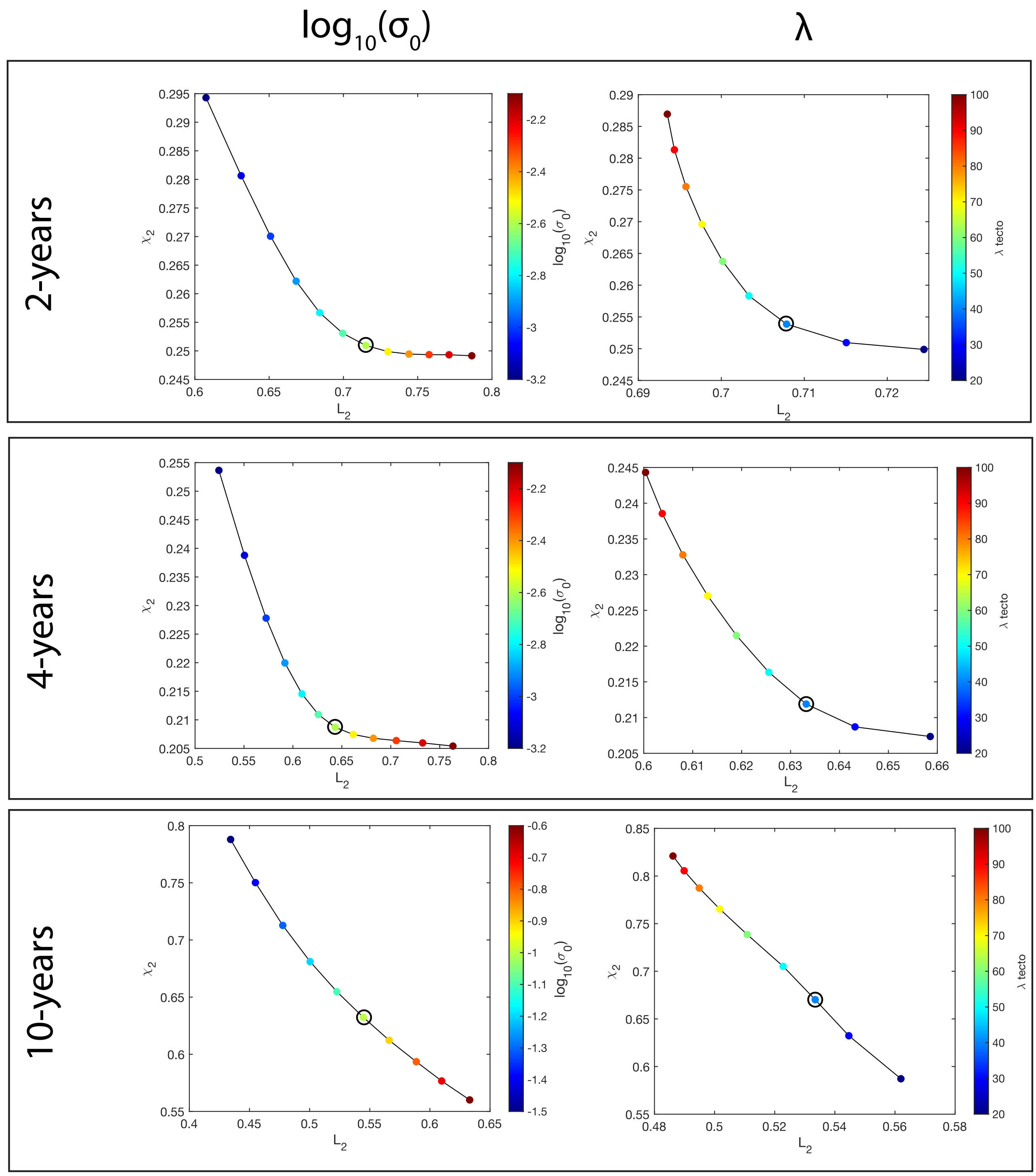

Figure S13. Parameters value optimization, data misfit (Chi-square χ^2) in function of the regularized solution (L2 norm) for different dampling values (left) and λ values (in km). On the left column is the dampling value σ_{m0} for a $\lambda = 50$km for the different period of observation. On the right column is the along strike correlation lenght (λ) for a $\sigma_{m0} = 10^{-2.6}$. The selected optimal model is circled in black.

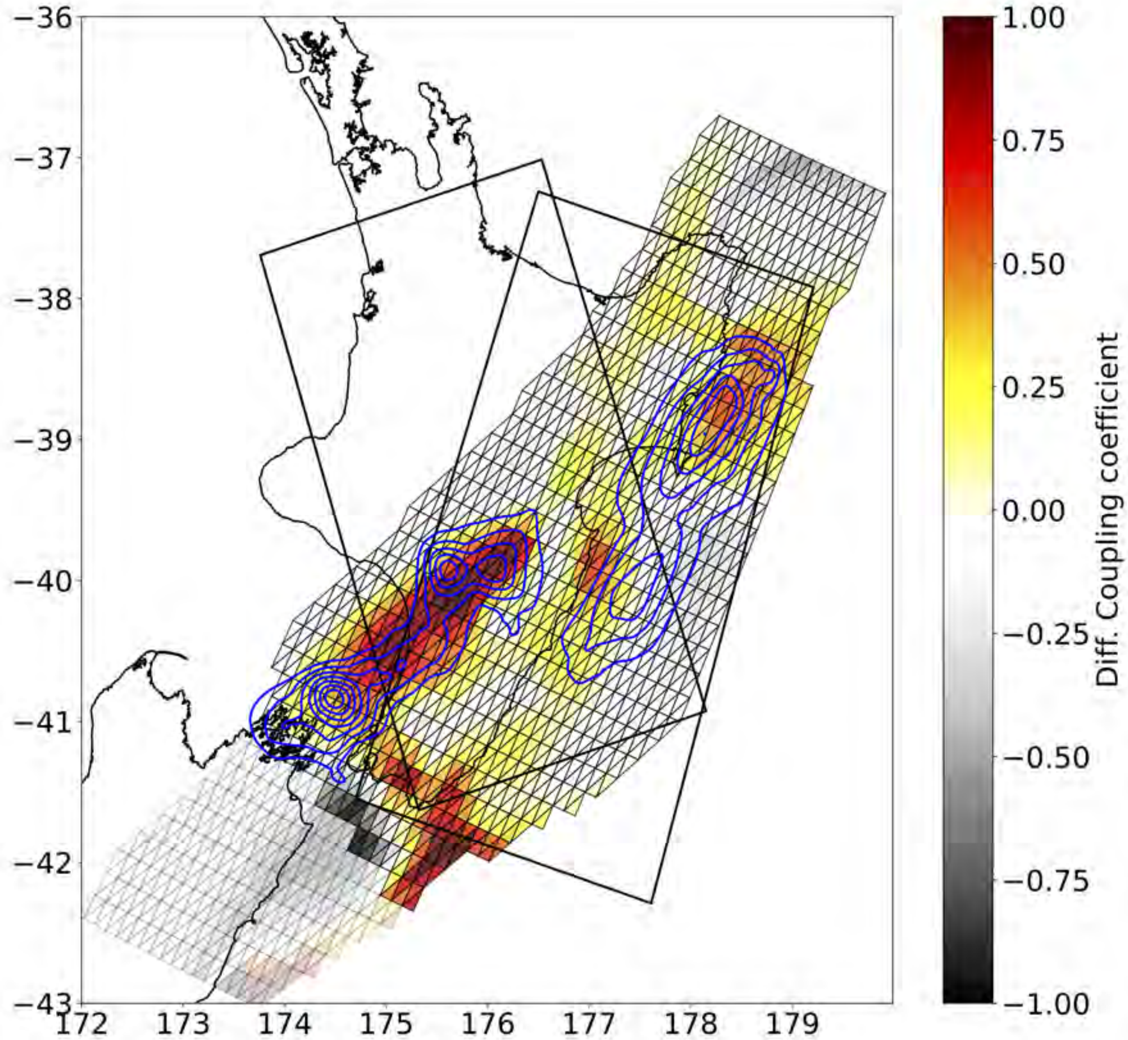

Figure S14. Difference of coupling coefficient between a coupling map over 2-years and 10-years. a positive value represent a region where the stress have been more accumulated during the short period than during the long period.